Expanding the Horizons for Viable Precursors and Liquid Fluxes for the Synthesis of $BaZrS_3$ and Related Compounds

Kiruba Catherine Vincent[*, a], Shubhanshu Agarwal[*, a], Zirui Fan[a], Alison Sofia Mesa Canizales[a,b], and Rakesh Agrawal[**, a]

[a]Davidson School of Chemical Engineering, Purdue University, West Lafayette, IN 47907(USA)
[b]Chemical and Environmental Engineering, Universidad Nacional de Colombia, Bogota D.C. (Colombia)

*Equal Contribution
**Corresponding author: Dr. Rakesh Agrawal. E-mail: agrawalr@purdue.edu

Keywords: Chalcogenide Perovskites, Solution-Processing, Low-Temperature, $BaZrS_3$, Transition Metal Chalcogenides, Metal sulfides, Metal halides

Abstract

Chalcogenide perovskites represent a prominent class of emerging semiconductor materials for photovoltaic applications, boasting excellent optoelectronic properties, appropriate bandgaps, and remarkable stability. Among these, $BaZrS_3$ is one of the most extensively studied chalcogenide perovskites. However, its synthesis typically demands high temperatures exceeding 900 °C. While recent advancements in solution-processing techniques have mitigated this challenge, they often rely on costly and difficult-to-find organometallic precursors. Furthermore, there is a notable gap in research regarding the influence of the Ba/Zr ratio on phase purity. Thus, our study explores solid-state reactions to investigate the impact of metal ratios and sulfur pressure on the phase purity of $BaZrS_3$. Expanding upon this investigation, we aim to leverage cost-effective metal halide and metal sulfide precursors for the solution-based synthesis of $BaMS_3$ (M=Ti, Zr, Hf) compounds. Additionally, we have devised a bilayer stacking approach to address the halide affinity of alkaline earth metals. Moreover, we introduce a novel solution-chemistry capable of dissolving alkaline earth metal sulfides, enabling the synthesis of $BaMS_3$ compounds from metal sulfide precursors. While the BaS_x liquid flux has shown promise, we identify the selenium liquid flux as an alternative method for synthesizing $BaMS_3$ compounds.

1. Introduction

Over the past two decades, there has been a notable surge in the development of new solar absorbers for photovoltaic applications. Lead halide perovskites have been particularly exciting due to their optoelectronic properties and the efficiencies they have achieved in photovoltaic devices.[1–3] However, they often suffer from increased instability to air, moisture, and heat, rendering them unsuitable for large-scale deployment in their current form.[4] Chalcogenide semiconductor materials, such as $Cu(In,Ga)Se_2$ and $Cu_2ZnSnSe_2$, have also shown promise as photovoltaic materials with suitable bandgaps for single-junction applications, but they lag behind lead halide perovskites in terms of efficiencies.[5,6] Nevertheless, these materials offer increased stability to air, moisture, and thermal degradation compared to lead halide perovskites.[7] They could also be readily mass-produced and deployed in photovoltaic farms, provided their device efficiencies are improved.

The possible research avenues in solar absorber research include improving the stability of halide perovskites, enhancing the device efficiencies of existing chalcogenide materials, or exploring stable, high-performing alternatives to lead halide perovskites. The latter has drawn the attention of the photovoltaic research community toward chalcogenide perovskites. These materials crystallize in a similar ABX_3 structure as lead halide perovskites, where A represents an alkaline earth metal (Ca, Sr, Ba), B denotes an early transition metal (Ti, Zr, Hf), and X is predominantly sulfur. While the Zr and Hf versions crystallize in a distorted perovskite structure, with the $[BX_6]^{2-}$ octahedra slightly tilted, the Ti versions crystallize in a distinct hexagonal structure.[8–10] Chalcogenide perovskites exhibit extremely high light absorption coefficients ($>10^5$ cm^{-1}), surpassing even lead halide perovskites, high dielectric constants, reasonable carrier mobilities, and strong photoluminescence.[8,11–13] Some of them feature suitable bandgaps for the top layer in tandem solar cell applications, while others show promise for solar water splitting and light-emitting diode applications.[8,12–15] $ATiS_3$ compounds possess a quasi-1-D structure with low thermal conductivity, making them promising candidates for thermoelectric applications.[16,17]

Despite their considerable promise, progress in researching these materials has been slow, primarily due to the high synthesis temperatures, often exceeding 900 °C.[12,18–21] Among these materials, $BaZrS_3$ has been the focus of much attention owing to its particularly suitable bandgap

for photovoltaic applications and its synthesis at relatively lower temperatures than other chalcogenide perovskites.[22,23] However, research on $BaZrS_3$ has predominantly centered on solid-state forms, with few reports on film synthesis, most of which rely on high-temperature vacuum deposition and annealing processes, which are less appealing.[23–26]

Recent studies from our group and others have made significant strides in lowering the synthesis temperature of $BaMS_3$ (M=Ti, Zr, Hf) compounds through moderate-temperature solution processing. These methods use a BaS_x liquid flux in a sulfur-rich environment but still rely on complex and expensive organometallic precursors for film casting.[27–31] Historically, solution-processed synthesis of chalcogenide materials has utilized cost-effective metal salts and metal sulfide precursors.[32–35] However, challenges such as the high oxophilicity of transition metals, the strong affinity of alkaline earth metals for halides, and the low solubility of alkaline-earth and transition metal sulfides in traditional solution chemistries have complicated these efforts.[30,36,37] A recent study from our group addressed the issue of oxophilicity by utilizing an HfH_2-based oxygen trap to remove oxide impurities from the film and the ampule environment during synthesis. [38] However, other challenges persist, requiring further investigation.

In this study, we have developed innovative approaches to address the halide affinity of alkaline-earth metals and synthesize $BaMS_3$ compounds from cost-effective metal halide precursors. We also demonstrate chemistry to dissolve alkaline-earth metal sulfides and propose a strategy to utilize metal sulfides for casting $BaMS_3$ films. Additionally, this study provides an example of using a selenium liquid flux, which could facilitate the synthesis of $BaMS_3$ and related compounds. Our study explores cost-effective solution-deposition routes for $BaMS_3$ synthesis by leveraging critical insights from previous reports.

2. Results and Discussion

2.1 Does $BaZrS_3$ allow off-stoichiometric compositions?

Chalcogenide semiconductors like $Cu(In,Ga)Se_2$ and $Cu_2ZnSnSe_4$ exhibit off-stoichiometry in their structure, where Cu-poor compositions up to a certain I/III or I/(II+IV) ratio do not induce phase segregation.[39,40] This is significant because Cu vacancies are shallow acceptor defects,

imparting p-type conductivity to these materials.[41] Notably, the record efficiency $Cu(In,Ga)Se_2$ device possesses a Cu/(In+Ga) ratio of 0.93.[42] Conversely, Cu-rich compositions often result in secondary Cu_2Se impurities, which may pose challenges if not easily eliminated.[41] This spurred our investigation into off-stoichiometric compositions in $BaZrS_3$, which remains largely unexplored. Similar to Cu-poor compositions in $Cu(In,Ga)Se_2$, Ba-poor compositions could potentially alter the carrier concentrations in $BaZrS_3$. The defects arising from such conditions, including V_{Ba}, Zr_{Ba}, S_{Ba}, and other defect complexes, warrant thorough examination. Preliminary indications from defect calculations suggest that these defects are either shallow or possess high defect formation energies. [43,44]

Table 1: Phases observed after sulfurization of BaS and ZrS_2 powder in the presence of sulfur at 575 °C for 12 h.

S. No.	Ba:Zr (Molar Ratio)	X-ray diffraction phases (Without water wash)	Raman phases (Without water wash)	Estimated sulfur pressure (atm)
1	2:1	$BaZrS_3 + BaS_3$	$BaZrS_3 + BaS_3$	0.79
2	1.5:1	$BaZrS_3 + BaS_3$	$BaZrS_3 + BaS_3$	0.79
3	1:1	$BaZrS_3$	$BaZrS_3$	0.79
4	0.9:1	$BaZrS_3$	$BaZrS_3$	0.79
5	0.8:1	$BaZrS_3$	$BaZrS_3$	0.79
6	0.7:1	$BaZrS_3$	$BaZrS_3$	0.79
7	0.6:1	$BaZrS_3 + ZrS_3$	$BaZrS_3 + ZrS_3$	0.79
8	0.5:1	$BaZrS_3 + ZrS_3$	$BaZrS_3 + ZrS_3$	0.79
9	0.4:1	$ZrS_3 + BaZrS_3$	ZrS_3	0.79
10	1.5:1	$BaZrS_3 + BaS_3$	$BaZrS_3 + BaS_3$	0.79
11	1.5:1	$BaZrS_3 + BaS_3$	$BaZrS_3 + BaS_3$	0.59
12	1.5:1	$BaZrS_3 + BaS_3 + Ba_3Zr_2S_7$	$BaZrS_3 + BaS_3 + Ba_3Zr_2S_7$	0.46

Table 1 enumerates the powder reactions where we mixed BaS and ZrS_2 in different molar ratios and sulfurized at 575 °C for 12 h in the presence of sulfur vapor. It is evident from **Table 1** and **Figure S1** that increasing the Ba:Zr ratio above 1 in the presence of excess sulfur led to the formation of the BaS_3 secondary phase alongside crystalline $BaZrS_3$. This indicates that $BaZrS_3$ does not accommodate Zr-poor off-stoichiometries, perhaps because V_{Zr} would disrupt the $[ZrS_6]^{2-}$ octahedra and destabilize the $BaZrS_3$ crystal lattice. It is plausible that in Ba-rich compositions, barium polysulfide was initially formed, but it decomposed into BaS_3 and sulfur upon cooling.[27] Consequently, crystalline BaS_3 and $BaZrS_3$ were observed under barium-rich conditions. Previous

studies have demonstrated the solubility of BaS_3 in water.[28] Thus, a gentle water wash could eliminate all BaS_3 impurities from the sample. In our investigation, we followed a water-washing procedure outlined in the experimental section, resulting in the phase-pure synthesis of $BaZrS_3$, as validated by X-ray diffraction in **Figure 1.a** and Raman spectroscopy in **Figure S2**. Regarding the Ba-poor compositions, no secondary phases were observed for Ba:Zr ~ 0.9, 0.8, and 0.7, yielding phase-pure $BaZrS_3$ as confirmed by X-ray diffraction and Raman spectroscopy. However, a further decrease to 0.6 metal ratio resulted in slight ZrS_3 impurities, evident in the X-ray diffraction spectra and Raman analysis (see **Figures 1.b and S3**). As the Ba:Zr ratio decreased, the prevalence of secondary phases increased as anticipated. Interestingly, our study indicates that $BaZrS_3$ can accommodate Ba-poor compositions up to Ba:Zr ~ 0.7. It would be intriguing to investigate the impact of these compositions on the optoelectronic properties, although this falls beyond the scope of our current work. The off-stoichiometry of $BaZrS_3$ could potentially impact the carrier concentration, which may vary depending on the Ba:Zr ratio in the material. Consequently, a wide range of carrier concentrations and both p-type and n-type conductivities have been reported for $BaZrS_3$.[12,45] Nevertheless, these findings will be helpful in the subsequent section, where we will elaborate on our approaches to fabricating $BaZrS_3$ films.

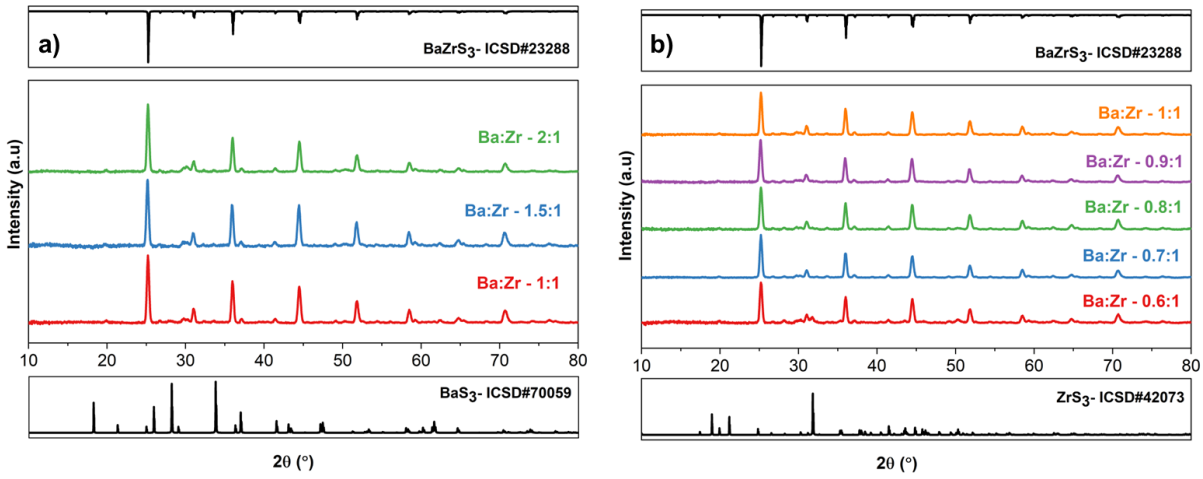

Figure 1. a) and b) X-ray diffraction pattern of the Ba-Zr-S powder synthesized with different Ba:Zr ratios at 575 °C for 12 h with a sulfur pressure of 0.79 atm. BaS and ZrS_2 were used as barium and zirconium precursors. The synthesized powders in a) were water-washed to remove any water-soluble impurities (BaS_3). The sample with Ba:Zr 0.6:1 in b) has ZrS_3 impurities.

It is essential to highlight that compositions with excess Ba under sulfur-poor conditions were also investigated. Despite the common expectation that Ruddlesden-Popper (RP) phases of $BaZrS_3$ would form in Ba-excess compositions due to their formation energies being similar to those of the perovskite phase [46], our previous discussion elucidated that $BaZrS_3$, along with BaS_3, was formed in Ba-excess compositions under sulfur-rich conditions. However, as the sulfur pressure decreased during synthesis, RP phases, notably $Ba_3Zr_2S_7$, reported to be the most stable among all Ba-Zr-S RP phases [45,47], emerged alongside $BaZrS_3$, as confirmed by X-ray diffraction and Raman spectroscopy (see **Figures S4 and S5**). At even lower sulfur pressures, starting binaries remained partially unreacted. Hence, it is imperative to operate under sulfur-excess conditions to achieve phase-pure $BaZrS_3$.

These observations indicate that, in a saturated sulfur environment with barium above stochiometric amount, $BaZrS_3$ does not accommodate Zr-deficient off-stoichiometric compounds. Instead, it leads to the formation of $BaZrS_3$ and BaS_3 secondary phases. Conversely, Ba-deficient off-stoichiometric compounds appear stable up to a Ba:Zr ratio of 0.7. Building on these findings, we have developed several solution processing routes for the synthesis of chalcogenide perovskites.

2.2. Stacked binary metal sulfides enabling the use of transition metal halides

Metal halides are widely available and relatively inexpensive, making them preferred precursors for many material systems. For instance, metal chlorides of certain late and post-transition elements, dissolved in dimethyl formamide (DMF) with thiourea as a sulfur source, can be utilized to synthesize metal sulfide semiconductors.[33,48] However, the affinity of barium and other alkaline earth metals for chlorine hindered our group's initial attempts to use these compounds in synthesizing $BaZrS_3$. As further confirmation, we investigated using a dimethylformamide ink containing $BaCl_2$, $ZrCl_4$, and thiourea. As anticipated, the resulting film contained $BaCl_2$ and ZrS_3 after sulfurization, as depicted in **Figure S6**, underscoring barium's affinity for chlorine. We encountered similar challenges with bromide and iodide precursors, discouraging using halides for mixed precursor inks. A potential alternative to bypass alkaline earth element's chlorine affinity involves employing a bilayer stacking approach with BaS_x/ZrS_x

films, where ZrS_x could be synthesized from zirconium halide precursors and then sulfurized to achieve $BaZrS_3$.

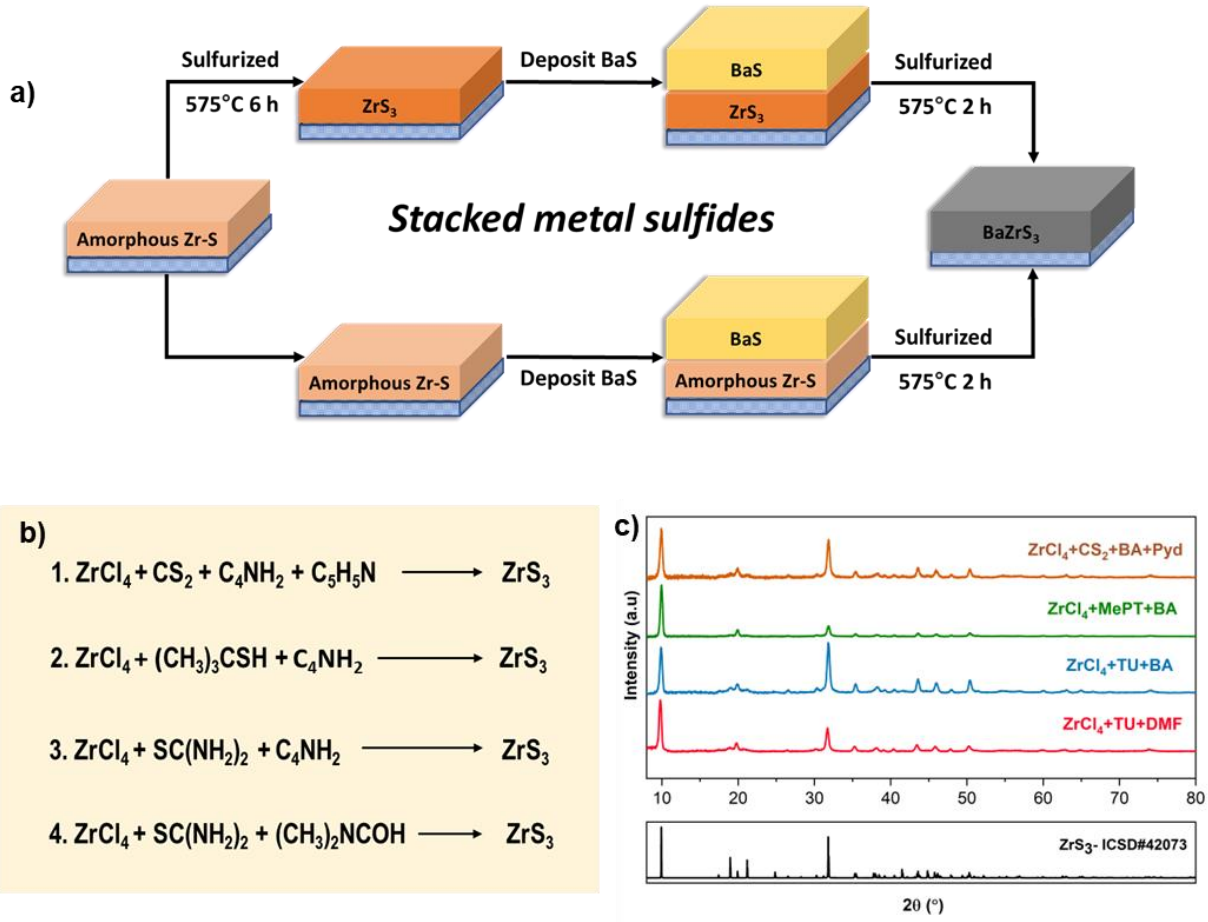

Figure 2. a) Reaction schematic depicting the synthesis of $BaMS_3$ by layering binary sulfides. b) Various molecular precursor chemistries employed for depositing ZrS_3 film. c) Plot comparing the X-ray diffraction patterns of ZrS_3 film prepared using different solution chemistries, (i) $ZrCl_4$ + thiourea (TU) + dimethyl formamide (DMF), (ii) $ZrCl_4$ + TU + butylamine (BA), (iii) $ZrCl_4$ + 2-methyl-2-propanethiol (MePT) + BA and (iv) $ZrCl_4$ + BA + CS_2 + pyridine (Pyd)

While some researchers previously regarded ZrS_3 as a dissociation product of $BaZrS_3$, our earlier suggestion posited ZrS_3 as a feasible zirconium precursor for synthesizing $BaZrS_3$.[27] In this scenario, ZrS_3 could undergo a reaction with BaS in the presence of excess sulfur, leading to the formation of $BaZrS_3$.[27] Based on this, our proposed method involves creating a binary sulfide stack with a bottom layer of ZrS_3 and a top layer of BaS, illustrated in **Figure 2.a**. Subsequently, this stack is heated in a sulfur-rich environment to yield $BaZrS_3$.

We dissolved Zr, Hf, and Ti halides using four distinct solution chemistries, resulting in metal-sulfur coordinated complexes, as depicted in **Figure 2.b**. The confirmation of metal-sulfur interactions in these chemistries was studied through liquid Raman and ^{1}H-NMR (Nuclear Magnetic Resonance) analyses. While amine-carbon disulfide chemistry has been extensively studied for dissolving various metal oxides, metal acetylacetonates, and metal hydroxides, limited research has focused on the dissolution of metal halides, particularly those of early transition metals. Liquid Raman analysis of a 0.3 M solution of $ZrCl_4$ in butylamine-CS_2-pyridine (**Figure S7**) revealed broadening of the C=S peak at 656 cm^{-1}, indicating potential metal-sulfur interaction, alongside a new peak at 2648 cm^{-1}, possibly attributed to the S-H bond from CS_2 insertion in butylamine. Similarly, for $ZrCl_4$ in 2-methyl-2-propanethiol-butylamine solution, **Figure S8** shows a slight shift and broadening in the C-S peak at 590 cm^{-1} and the S-H peak at 2577 cm^{-1}, indicating sulfur coordination to the zirconium through a dative bond.[49] However, the observed peak shift was minimal, and the ratio of the S-H peak to the C-S peak did not decrease significantly, suggesting incomplete substitution of chlorine with thiolate due to thiolate formation. This finding aligns with observations by Murria et al., who reported similar incomplete substitution when dissolving copper chlorides in amine-thiol systems.[32]

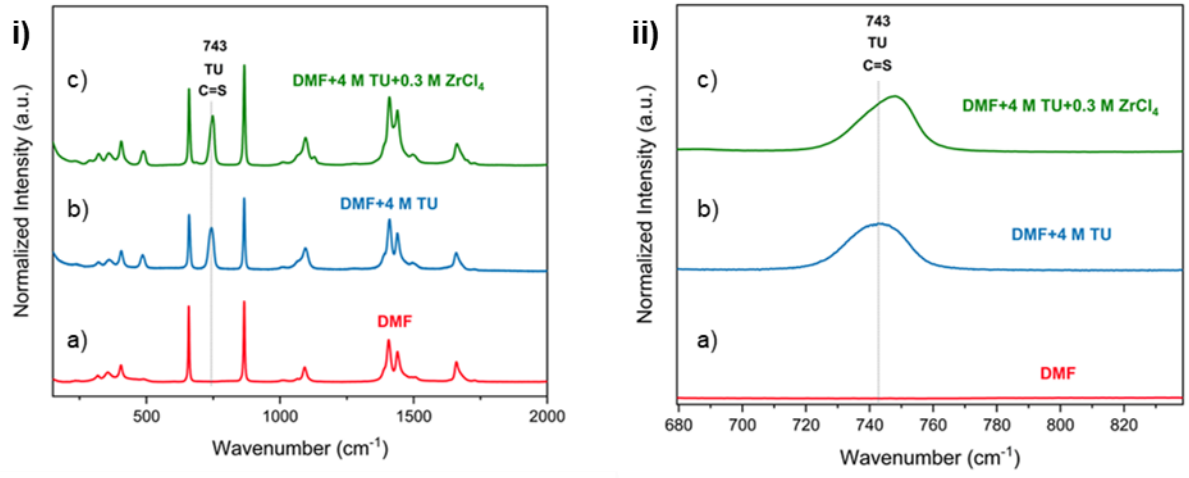

Figure 3. Liquid Raman on only a) dimethyl formamide (DMF), b) thiourea (TU)+DMF, and c) TU+DMF+$ZrCl_4$ (0.3M). The peak shift in the C=S bond stretch of TU suggests a metal-sulfur interaction. ii) presents the zoomed-in representation of i).

^{1}H-NMR studies also show a likely metal-sulfur interaction between $ZrCl_4$ and thiol (**Figure S9**). The Zr-Cl-thiolate, however, did not dissolve significantly in pyridine-d_5 initially. But, adding a stoichiometric amount of butylamine resulted in complete dissolution with a broadening in the

^{1}H-NMR peak of H bounded to sulfur, hinting towards some interaction between butylamine and 2-methyl-2-propanethiol likely forming $[CH_3(CH_2)_3NH_4]^+[SC(CH_3)_3]^-$. The ^{1}H-NMR results in **Figure S10** show the broadening of the thiol proton peak after adding $ZrCl_4$, but the peak did not disappear. Notably, exchangeable protons, such as those in the thiol group, are not always accurately quantified through peak integration. The peak broadening indicates a dynamic thiol proton. We hypothesize that this suggests the thiolate is in equilibrium between its protonated and deprotonated forms. When it is deprotonated, we expect it to be bound to the Zr^{4+}. This observation could also indicate that not all Zr-Cl bonds underwent replacement with thiol; alternatively, it might have resulted in the formation of an adduct.

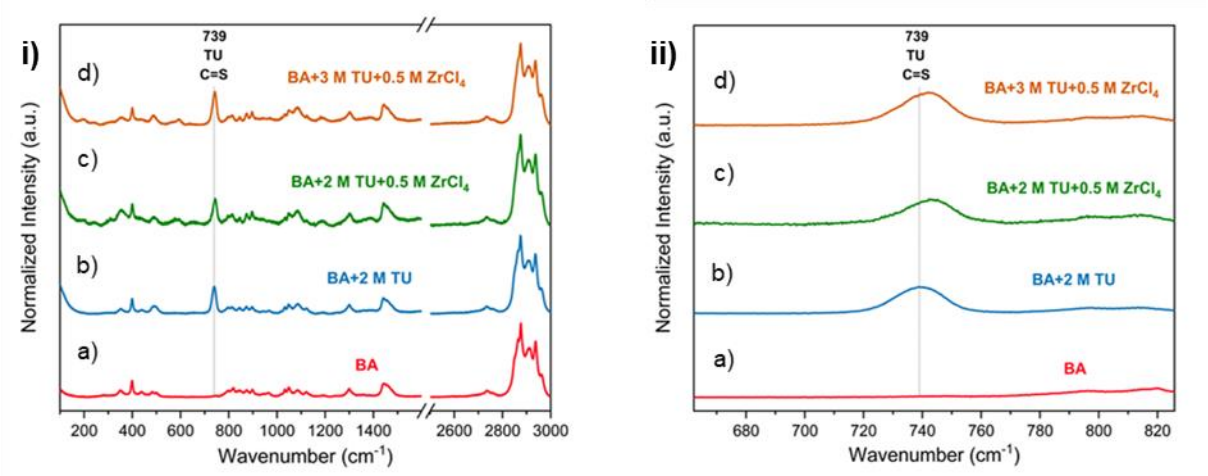

Figure 4. Liquid Raman on only a) butylamine (BA), b) thiourea (TU)+BA, c) TU (2M)+BA+$ZrCl_4$ (0.5 M), and d) TU (3M)+BA+$ZrCl_4$ (0.5 M). The peak shift in the C=S bond stretch of TU suggests a metal-sulfur interaction. ii) presents the zoomed-in representation of i).

Interactions were also observed in the $ZrCl_4$-thiourea-dimethyl formamide and $ZrCl_4$-thiourea-butylamine systems, leading to shifts and broadening in the C=S Raman peak, as illustrated in **Figures 3 and 4**. Similar dissolutions can also be achieved with $ZrBr_4$ and ZrI_4, yielding soluble complexes. All four Zr-S coordinated solutions were then doctor blade-coated onto alumina-coated Eagle XG glass substrates and annealed at 350 °C on a hot plate to remove the excess solvent, resulting in an amorphous ZrS_x compound. Subsequently, the resulting film underwent sulfurization in an ampule containing HfH_2 and sulfur for 6 h at 575 °C to form a ZrS_3 film, as depicted in the X-ray diffraction patterns and Raman spectra in **Figures 2.c and S11**. The role of HfH_2 in removing any residual oxygen in the film is elaborated in our previous work.[38] It is important to note that although ZrS_3 could be synthesized at much lower temperatures of 475 °C,

we chose 6 h at 575 °C to ensure complete removal of residual oxygen (see **Figure S12**). Further optimization strategies such as rigorous solvent drying, use of anhydrous precursors, processing in ultra-oxygen-free glove boxes, and avoiding exposure to air during the entire processing could significantly reduce the synthesis time and temperature. The X-ray diffraction patterns and Raman spectroscopy confirmed the production of phase-pure ZrS_3 in all cases. The secondary phase of ZrO_2 was eliminated with prolonged sulfurization time and careful handling of precursors and solutions. Similar to previous studies, the ZrS_3 films exhibited non-continuous morphology due to the ribbon structure of ZrS_3 (refer to **Figures 5.b, S13, and S14**).[38] Energy Dispersive X-ray Spectroscopy (EDX) maps in **Figures S15 and S16** confirm the uniform distribution of Zr and S in the grains. Furthermore, ZrS_3 synthesis from soluble inks of $ZrBr_4$ and ZrI_4 was also demonstrated (see **Figure S17**). It is worth noting that after annealing the film on the hot plate, trace amounts of residual chlorine, bromine, or iodine were detected in the film via X-ray Fluorescence measurements, but no halide impurities remained after sulfurization.

Subsequently, a thin layer of BaS was coated onto these ZrS_3 films using the soluble barium thiolate ink obtained by dissolving Bis(pentamethylcyclopentadienyl) barium (Cp^*_2Ba) in 2-methyl-2-propanethiol and butylamine (see experimental section for details), and the resulting stacked film of BaS/ZrS_3 was sulfurized with sulfur and HfH_2. The as-annealed stacked films exhibit crystalline phases of both BaS and ZrS_3, as depicted in **Figures 5.a and S18**. While care was taken to ensure that approximately equal amounts of Ba and Zr molar ratios were present in the film by maintaining similar concentrations of Ba and Zr inks, previous discussions in the study indicate that a barium-excess film could also be utilized. This is because it would form $BaZrS_3$ and BaS_3 upon sulfurization, and the BaS_3 component could be easily washed away. During sulfurization at 575 °C, this process utilized the BaS_x liquid flux to accelerate mass transfer, and although shorter times should be feasible, sulfurization was performed for 2 h to minimize undesirable oxide phases. As illustrated in **Figures 5.a, S18, and S19**, we obtained a pure $BaZrS_3$ phase, as confirmed by X-ray diffraction and Raman spectroscopy. The diffuse reflectance spectroscopy also confirmed a bandgap of around 1.85 eV (see **Figure S20**). Nevertheless, the film exhibited cracking and isolated grains (see **Figures 5.c and S21**), suggesting a need for further research to optimally control the BaS_x liquid flux. However, this could be an enticing way to make micron-scale single crystals without residual impurities. EDX analysis confirmed the uniform distribution of Ba, Zr, and S, as shown in **Figures S22 and S23**. Additionally, the $BaZrS_3$ grains

show no residual chlorine (See **Figure S24**). This versatile method can be readily applied to Ba-Hf-S and Ba-Ti-S systems, yielding $Ba_6Hf_5S_{16}$ and $BaTiS_3$, as demonstrated in **Figures S25, S26, and S27**. However, achieving stoichiometric $BaHfS_3$ using this route proved challenging due to the competing Ruddlesden-Popper phases of the Ba-Hf-S system. In all the cases, an equal number of layers with equally concentrated barium and zirconium/hafnium/titanium solutions were blade-coated to ensure a nearly stoichiometric film.

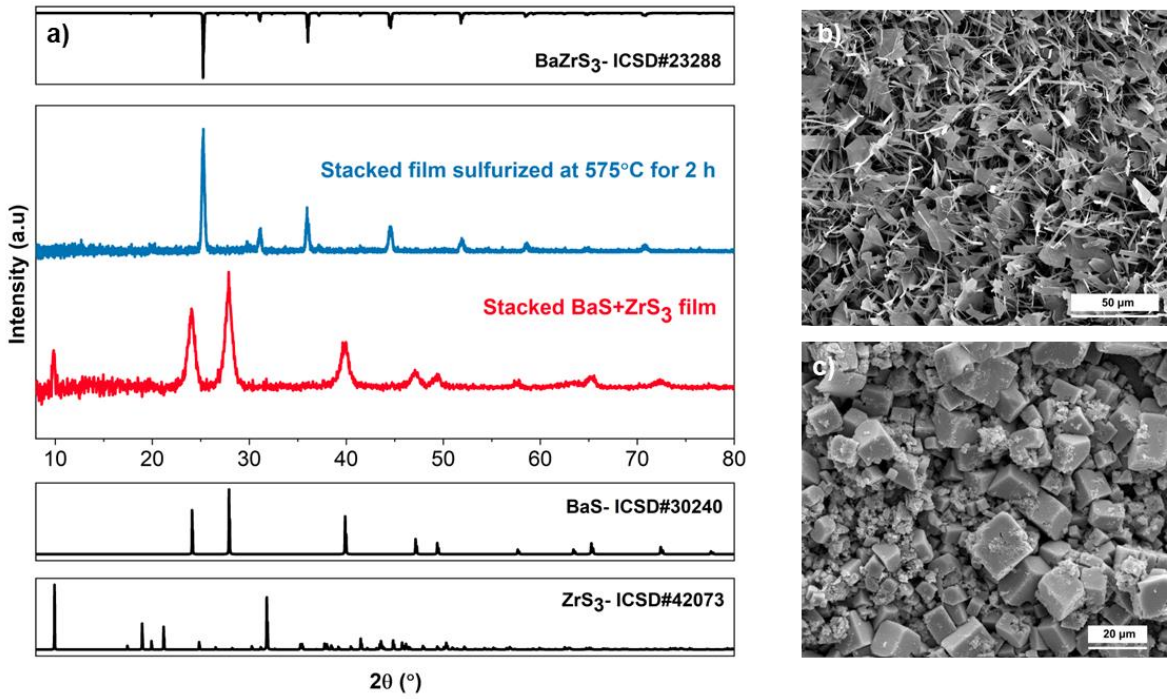

Figure 5. a) X-ray diffraction pattern showcasing the as-annealed stacked bilayer film of ZrS_3 and BaS before ampule sulfurization and the $BaZrS_3$ film after sulfurization. b) SEM top-view image depicting the ZrS_3 film prepared from the $ZrCl_4$-butylamine-CS_2-pyridine solution chemistry. c) SEM top-view image illustrating the $BaZrS_3$ film derived from the ZrS_3-BaS bilayer stack.

The success of this approach is noteworthy as it enables the utilization of easily manageable and cost-effective halide precursors. While our primary focus was on one stacking method utilizing the halide precursors, alternative approaches could also be explored. In another instance, we applied a $ZrCl_4$-containing ink at the bottom to form an amorphous ZrS_x layer without sulfurizing it to ZrS_3. The coated film underwent annealing at 450 °C for 30 minutes to eliminate residual chlorine. Subsequently, BaS was applied to the top using the barium thiolate solution, and the stacked film was sulfurized, resulting in $BaZrS_3$, as shown in **Figure S28**. In an alternate scenario, BaS was coated at the bottom, and $ZrCl_4$-containing ink was applied at the top. After annealing

and sulfurization of this stack, $Ba_3Zr_2S_7$ was obtained, albeit with significant secondary phases, including $BaCl_2$ and ZrS_3, as illustrated in **Figure S29**. This outcome was anticipated, as barium likely reacted with chlorine during the annealing process of the stacked film on the hot plate. These findings underscore the significance of selecting suitable precursors and optimizing the sequence of processing steps to establish a thermodynamic driving force for synthesizing chalcogenide perovskites.

2.3 Hybrid Colloidal Molecular Precursor Inks

In addition to pure metals, metal chalcogenides are preferred as low-cost, anionic, impurity-free metal precursors for solution-processed chalcogenide thin films.[50,51] Employing metal sulfides as precursors for synthesis would restrict the incorporation of unwanted anionic impurities and offer a cost-effective, streamlined route to synthesize $BaMS_3$ compounds. However, the dissolution of alkaline earth metal sulfides and transition metal sulfides has historically been challenging, with no reports of ZrS_2 or ZrS_3 dissolution in any solution chemistry and only one report on co-dissolution of BaS alongside Cu_2S and SnO in ethylenediamine-ethanedithiol (EDA-EDT) at 60 °C for 11 days.[52] This dissolution was arduous, and attempts to dissolve only BaS in EDA-EDT were unsuccessful in our experiments, even after multiple attempts. Consequently, further investigation was necessary to identify solution chemistry capable of dissolving alkaline earth metal sulfides. As a result, various combinations of amine-thiol with different concentrations were explored, yet no success was achieved in room-temperature dissolutions. Notable solution chemistries such as hydrazine-sulfur also failed to dissolve BaS and ZrS_2.

However, combining amine and CS_2 to produce alkyldithiocarbamic acid opened new possibilities for reactive solvent systems as we investigated this less-studied chemistry. Previously, butyldithiocarbamic acid had been shown to dissolve metal salts such as metal oxides,[34] but we notably extended this chemistry by dissolving alkaline earth metal sulfides in propyldithiocarbamic acid in pyridine, resulting in a clear solution. This marks the first instance of standalone dissolution of BaS and SrS in solution chemistry and could play a pivotal role in the solution-processed synthesis of several alkaline earth metal-based chalcogenide compounds, including $BaMS_3$ chalcogenide perovskites, Cu_2BaSnS_4, and Cu_2SrSnS_4. As a side note, due to the current interest in forming thin films of Cu_2BaSnS_4 for solar cells[53,54], we demonstrate solution-

deposited synthesis of Cu_2BaSnS_4 using this chemistry in **Figure S30**, where we co-dissolved Cu_2S, BaS, and Sn in propylamine-CS_2-pyridine to create a mixed precursor ink.

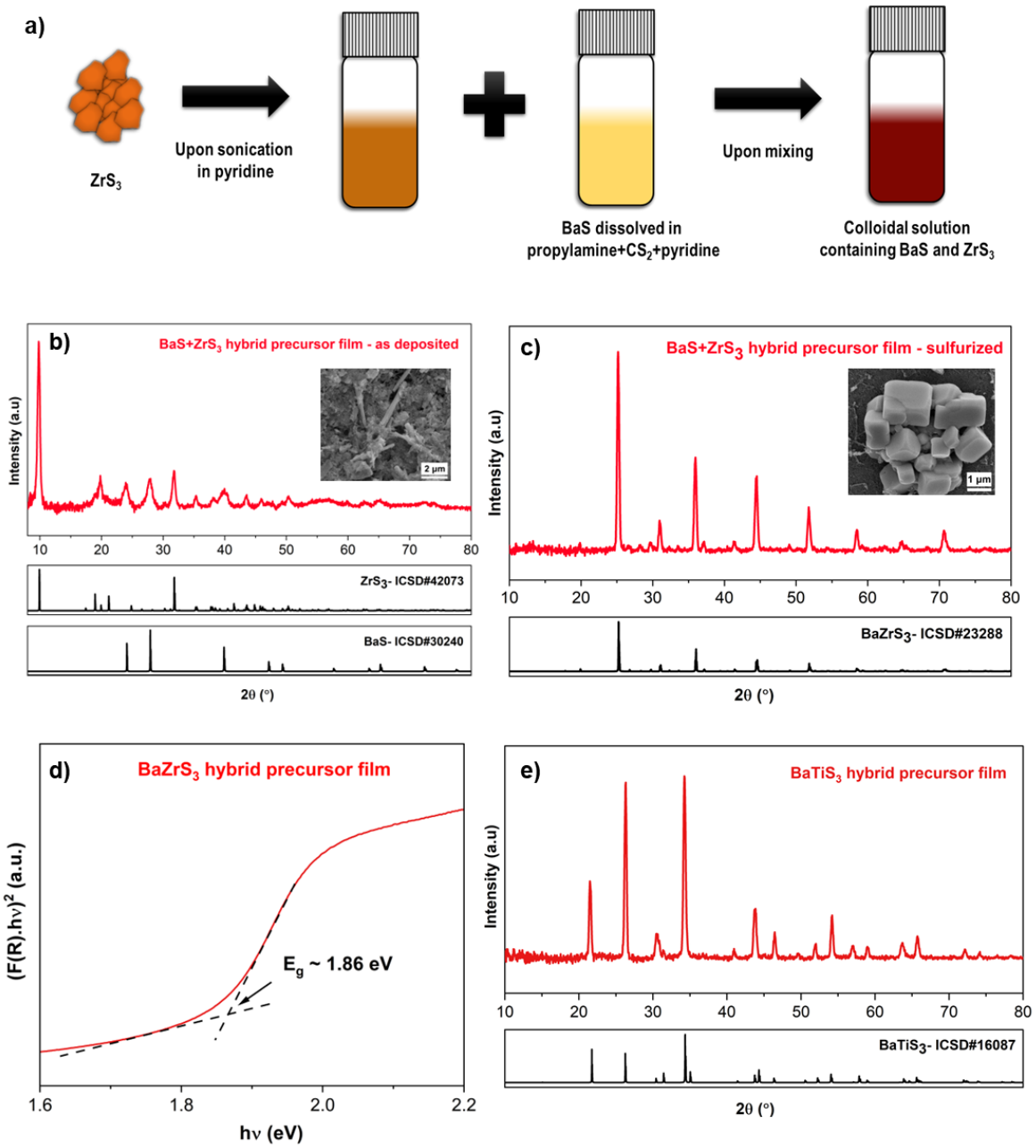

Figure 6. a) Reaction schematic illustrating the preparation process of a hybrid colloidal molecular precursor ink using binary metal sulfides. b) X-ray diffraction pattern of the as-coated hybrid precursor film, with an inset displaying the SEM top view of the as-annealed film. c) X-ray diffraction pattern of the $BaZrS_3$ film obtained after the sulfurization of the as-coated film, with an inset showing the SEM top view of the sulfurized film. d) Kubelka-Munk transformation applied to the diffuse reflectance spectra of the $BaZrS_3$ film derived from hybrid precursor film (considering direct bandgap)[8] e) X-ray diffraction pattern of the $BaTiS_3$ film obtained after sulfurizing the as-coated BaS-TiS_2 film from the hybrid precursor route.

While our newly enhanced solution chemistry for BaS could be used with the previously described routes for homogeneous precursor inks and stacked films as Ba source, here we describe a new hybrid molecular precursor route employing dissolved BaS and colloidal suspension of ZrS_3. ZrS_2 and ZrS_3 are Van der Waals bonded 2D materials, suggesting the potential for colloidal suspensions in a suitable solvent. However, ZrS_2 is prone to oxidation upon exposure to air, prompting us to utilize ZrS_3 as the Zr precursor. Compared to a complete molecular precursor approach, colloidal particles in ink could facilitate nucleation in the coating process, leading to favorable film morphology. The hybrid molecular precursor route featuring dissolved BaS in an amine-CS_2 reactive solvent system with pyridine as the bulk solvent and colloidal ZrS_3 flakes dispersed also builds upon the concept of ZrS_3 as a plausible precursor outlined in our previous publication.[27] The resulting ink underwent sonication for several days to achieve a homogeneous dispersion solution, with the Ba:Zr ratio adjusted to be stoichiometric. Subsequently, the ink was coated and sulfurized (refer to **Figure 6.a** for a schematic of the synthesis process). Despite the reasonable air stability of BaS and ZrS_3, the solution was coated in an oxygen-free glovebox in this study. The as-coated film contained both BaS and ZrS_3, as confirmed in **Figure 6.b**, and upon sulfurization, this method yielded phase-pure $BaZrS_3$ at 575 °C (refer to **Figure 6.c and Figure S31**). EDX measurements of this film (depicted in **Figure S32**) verified the presence of Ba, Zr, and S in the grains. However, we observed that the size of the ZrS_3 colloidal particles influenced the reaction time. In one instance, ZrS_3 powder was synthesized by sulfurizing Zr nanopowder, while in another case, bulk ZrS_2 powder was sulfurized to form ZrS_3 powder, both at 575 °C for 18 h. The average grain size of ZrS_3 produced from Zr nanopowder was significantly smaller than that from ZrS_2 powder, resulting in a faster reaction to form $BaZrS_3$. With the larger ZrS_3 particles, we observed some unreacted BaS_3 and ZrS_3, along with $BaZrS_3$, in the film (refer to **Figure S33**). However, in both scenarios, the targeted continuous thin film was not achieved, leading to the formation of isolated large grains of $BaZrS_3$ (as indicated in the inset of **Figure 6.c and Figure S34**) rather than the intended continuous thin film. As previously noted, the overgrowth to form material islands is a common challenge for methods relying on a BaS_x liquid flux. Therefore, controlling the quantity of liquid flux is crucial for this approach. Additionally, an alternative synthesis of ZrS_3 to produce smaller particles in the suspension could further decrease reaction time and improve film morphology. Nevertheless, the diffuse reflectance measurements confirmed a bandgap of 1.86 eV for the $BaZrS_3$ film, promising its potential utilization in tandem solar cell

applications (depicted in **Figure 6.d**). Notably, this method was successfully extended for synthesizing related chalcogenide perovskite $BaHfS_3$ and hexagonal $BaTiS_3$, as confirmed by the X-ray diffraction and Raman spectra (see **Figures 6.e, 7.a, S35 and S36**). Moreover, the diffuse reflectance indicated a bandgap of approximately 2.16 eV for $BaHfS_3$, promising its potential utility in optoelectronic applications (shown in **Figure 7.b**).

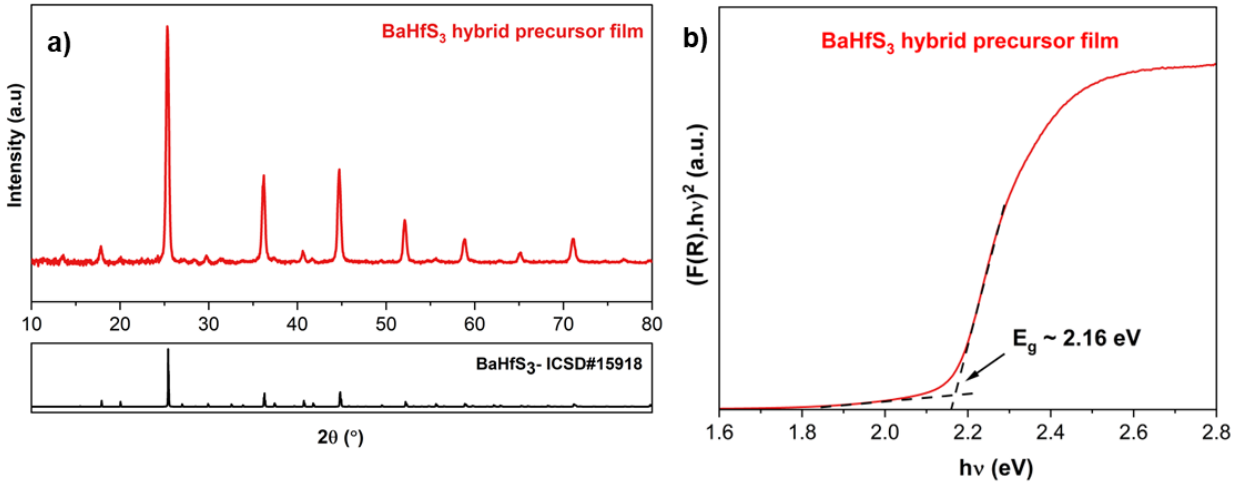

Figure 7. a) X-ray diffraction pattern of the $BaHfS_3$ film obtained after sulfurizing the as-coated BaS-HfS_3 film from the hybrid precursor route. a) Kubelka-Munk transformation applied to the diffuse reflectance spectra of the $BaHfS_3$ film derived from hybrid precursor film (considering direct bandgap).[8]

This study represents the first account of a pathway solely employing metal sulfide precursors for the solution-processed synthesis of $BaZrS_3$ and other related compounds. Furthermore, the dissolution of BaS in propylamine-CS_2 exhibits novelty. Subsequent studies could explore solution chemistry aimed at co-dissolving BaS and ZrS_2/ZrS_3 to establish a fully dissolved molecular precursor route, which would also aid in limiting excess BaS_x flux and controlling grain growth.

2.3. Utilizing selenium liquid flux: solid-state synthesis of $BaMS_3$

From the above discussions, it is evident that a liquid flux is paramount in synthesizing chalcogenide perovskites at lower temperatures. BaS_x liquid flux has been pivotal in the previously discussed solution-processing routes for synthesizing $BaMS_3$ compounds. This section explores other potential liquid fluxes for synthesizing $BaMS_3$ and related compounds. Prior studies on chalcogenide materials have employed various liquid fluxes to lower synthesis temperatures. Examples include $Cu_{2-x}Se$ flux in Cu-based chalcogenide semiconductors, Sb_2S_3 liquid flux in

antimony-based semiconductors, and BaS_x in barium-based chalcogenide semiconductors. [27,29,55–57] As mentioned earlier, an ideal liquid flux should meet strict requirements: it should be in a liquid state at the reaction temperature, partially dissolve the metal precursors to reduce diffusion barriers, and avoid reacting with precursors to form undesired secondary phases. A selenium liquid flux can likely fulfill these requirements—it remains liquid above 220 °C, partially dissolves metal sulfides, and the instability of $BaMSe_3$ compounds could potentially prevent the formation of ternary selenide secondary phases. As a proof of concept, solid-state samples were synthesized by combining BaS, ZrS_2, and elemental Se in a sealed ampule and heating to a target temperature (refer to **Figure 8.a**). X-ray diffraction measurements from samples quenched at different temperatures showed that BaS and ZrS_2 dissolved in the selenium liquid, as evidenced by the absence of BaS diffraction peaks at 475 °C and diminished ZrS_2 peaks. However, the emergence of $BaSe_3$ peaks indicated the partial breakdown of BaS to form $BaSe_3$. As the temperature increased to 530 °C, intense peaks of $BaZrS_3$ were observed, accompanied by a diminished secondary phase of $BaSe_3$. This increase in $BaZrS_3$ intensity continued to 575 °C, see **Figure 8.b**. One hypothesis for this success is that BaS and ZrS_2 do not significantly break down into BaSe/$BaSe_3$ and $ZrSe_2$/$ZrSe_3$ at the temperatures used. If they did, at least some byproduct sulfur would have escaped to the vapor phase, resulting in insufficient sulfur for $BaZrS_3$ formation. The absence of significant binary selenides supports this hypothesis—binary sulfides simply dissolve as binaries and reconstitute as $BaZrS_3$ without the need for additional sulfur in the mixture.

With increased reaction time, the relative peak intensity of $BaZrS_3$ to $BaSe_3$ continued to rise, albeit with a small amount of residual $BaSe_3$ secondary phase remaining after 24 h of reaction at 575 °C. This residual $BaSe_3$ was found to be readily soluble in water. Consequently, the $BaZrS_3$ powder, containing the $BaSe_3$ secondary phase, underwent two rinses with deionized water to achieve a pure $BaZrS_3$ phase, as confirmed by X-ray diffraction analysis (see **Figures 8.c**). Interestingly, in the absence of excess sulfur and the presence of a liquid flux, $BaZrS_3$ formed instead of the Ruddlesden-Popper phase. This finding and previous results in this study suggest that Ruddlesden-Popper phases form in a sulfur-poor environment only when there are diffusional limitations. However, Raman analysis in **Figure S37** suggested the presence of residual melt from the selenium liquid flux, encapsulating the $BaZrS_3$ grains. EDX analysis of the water-washed $BaZrS_3$ powder further supported this observation. The $BaZrS_3$ powder exhibited lumping and possibly contained agglomerates of finer $BaZrS_3$ grains in the nanometer range, as depicted in

Figure S38, with small selenium-rich regions illustrated in **Figure S39**. However, this excess selenium could be readily dissolved in various solution chemistries, with amine-thiol mixtures and trioctylphosphine being some solvents.[58,59] **Figure S40** highlights our attempt to dissolve this residual selenium. Notably, compositional analysis of the $BaZrS_3$ powder revealed negligible selenium content (see **Figure S41**).

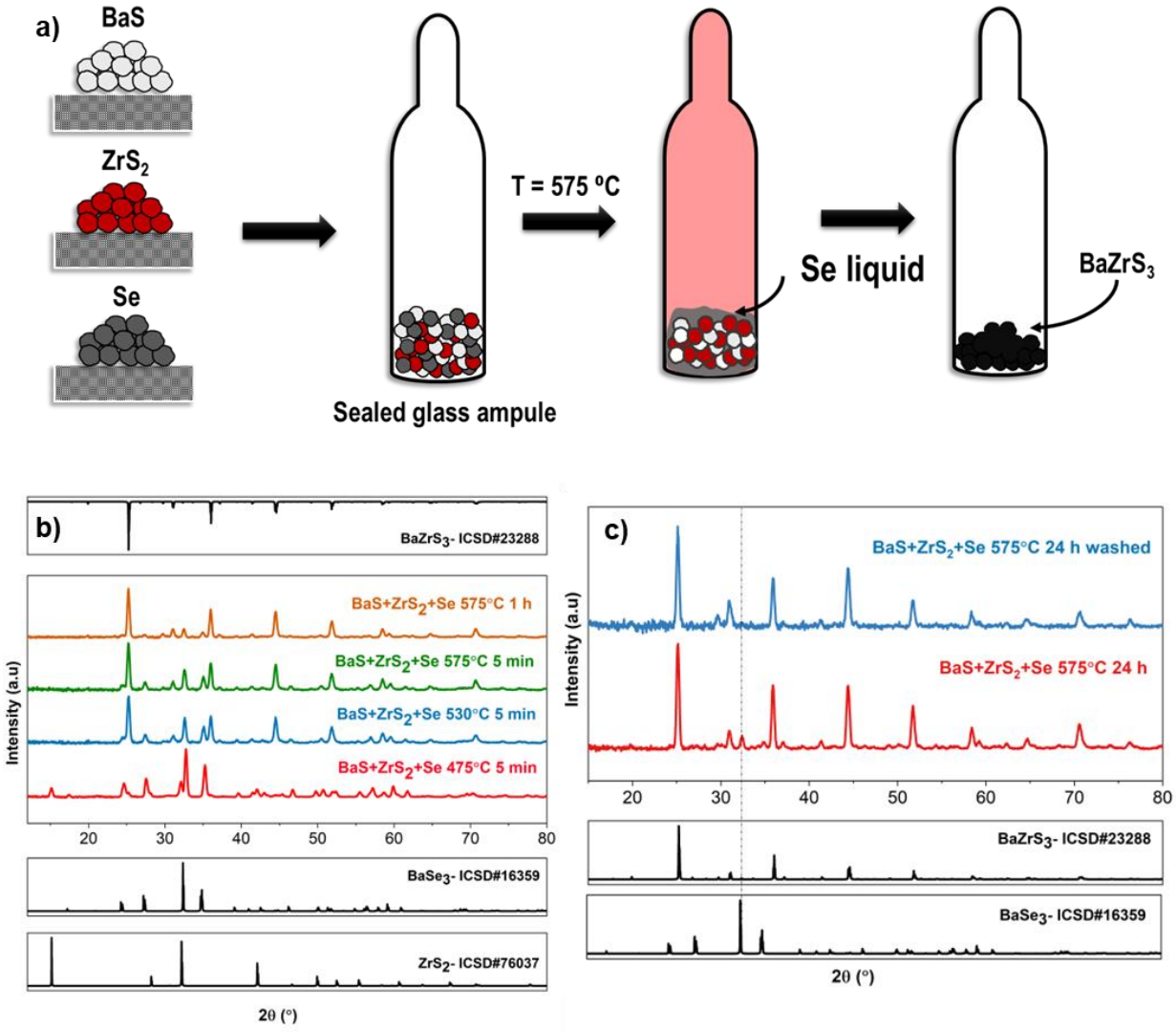

Figure 8. a) Reaction schematic depicting the synthesis of $BaMS_3$ utilizing a selenium liquid flux. b) X-ray diffraction patterns illustrating the evolution of intermediate phases with temperature for binary sulfides when subjected to the selenium liquid flux. c) Comparison plot of the X-ray diffraction pattern for the water-washed and unwashed $BaZrS_3$ powder.

A similar procedure led to the synthesizing of ternary perovskite $BaHfS_3$ and hexagonal $BaTiS_3$, as evidenced in **Figures S42-S45**. This approach's success lies in synthesizing sulfide perovskites

and in the potential for selenium alloying at moderate temperatures by heating a mixture of BaS, ZrS_2, Zr, and selenium powder together. However, this process would require optimization and, therefore, would be investigated as part of a separate study. Although $BaMS_3$ compounds have been successfully synthesized at temperatures below 600 °C, attempts to synthesize $SrMS_3$ compounds via sulfurization of respective binary sulfides with excess sulfur have not yielded successful results (see **Figure S46**). One reason could be that, unlike BaS_x liquid flux at temperatures above 525 °C, Sr has not been reported to form any liquid strontium polysulfides at temperatures below 600 °C.

When the binary sulfides of strontium and zirconium were heated with selenium at 575 °C, we observed the emergence of α-$SrZrS_3$ peaks (needle-like crystal structure), as depicted in **Figure S47**. However, achieving phase pure α-$SrZrS_3$ proved to be difficult in this case. It should be noted that single crystal analysis on a similar sample subjected to 650 °C revealed a striking similarity in the diffraction pattern between α-$SrZrS_3$ and the somewhat unlikely compound $SrSeS_3$. Rigorous elemental characterizations are needed in the future to differentiate between these phases accurately. We noted a gradual increase in peak intensity from 48 h to 7 days and 21 days, as illustrated in **Figure S47**. These results are promising and encourage further exploration of other liquid fluxes. Moreover, this outcome underscores the utility of selenium liquid flux and highlights that the synthesis of Sr ternaries might be thermodynamically favorable at these temperatures but suffers from diffusional limitations.

3. Conclusions

Chalcogenide perovskites, while promising, have posed challenges in the synthesis, hindering progress in this material system. $BaZrS_3$, particularly suitable for photovoltaic applications, has been synthesized at temperatures unsuitable for solar cell integration. Our study aimed to ascertain the optimal metal ratios and sulfur pressure during the synthesis of $BaZrS_3$ to prevent phase disintegration. Subsequently, we proposed methods to address limitations arising from the halide affinity of alkaline earth metals and the unavailability of solution chemistries for alkaline earth metal sulfides to fabricate solution-deposited $BaZrS_3$ thin films.

We successfully dissolved alkaline earth sulfides such as BaS and SrS, demonstrating their utility in synthesis. Additionally, we showcased the successful synthesis of $BaMS_3$ by employing stacked films of appropriate precursors. Notably, the sequencing of stacked layers allowed the use of $ZrCl_4$ precursor without forming $BaCl_2$ impurity in the final $BaZrS_3$ film. Furthermore, we identified an alternative liquid in Se that facilitates the formation of $BaMS_3$ at temperatures below 600 °C. The versatility of our methods extends to the synthesis of other $BaMS_3$ (M=Hf, Ti) compounds, enabling low-cost and facile production of this class of chalcogenide perovskites.

4. Experimental Methods

4.1 Materials and Characterization

Barium sulfide (BaS, 99.9%), titanium (IV) sulfide (TiS_2, 99.9%), selenium powder (99.99%), zirconium (IV) chloride ($ZrCl_4$, anhydrous powder, >99.99%), hafnium (IV) chloride ($HfCl_4$, purified by sublimation, 99.9), 2-methyl-2-propanethiol (MePT, 99%), butylamine (BA, 99.5%), carbon disulfide (CS_2, anhydrous, >99%), pyridine (Pyd, anhydrous, 99.8%), N-N dimethyl formamide (DMF, anhydrous, 99.8%), thiourea (TU, ACS Reagent, >99%), sulfur flakes (>99.99%), molecular sieves (Type 3A, bead size 8-12 mesh), propylamine (PA, >99%) and alumina dispersed in isopropanol (20 wt%) were purchased from Sigma Aldrich. Bis(pentamethylcyclopentadienyl)barium (Cp^*_2Ba), Zirconium (IV) sulfide (ZrS_2, 99%), zirconium (IV) bromide ($ZrBr_4$, 98%) and zirconium (IV) iodide (ZrI_4, 99.5 %) were purchased from STREM chemicals. Titanium (IV) Chloride ($TiCl_4$, 99.99%) and pyridine-d{5} (99.5% Isotopic) were purchased from Fisher Scientific. Titanium hydride (99.9%) and hafnium hydride (99.9%) were purchased from Nano Research Elements. Borosilicate glass ampules were procured from Chemglass. Hafnium disulfide (>99.995%) was purchased from Ossila.

Solvents without sure seal were stored over molecular sieves for several days before use. Thiourea was recrystallized through a two-step process, using 18.2 MΩ deionized water and was dried under vacuum overnight. All other chemicals were used as received.

Alkali-free Eagle XG glass substrates were purchased from Stemmerich. It should be noted that the glass substrate itself contains traces of zirconium. Selenium powder was vacuum dried at 100 °C overnight before use. Sulfur flakes were finely ground inside a nitrogen-filled glovebox and vacuum-dried overnight at room temperature. All chemicals were stored in nitrogen-filled glove boxes. Sulfurization at 650 °C was carried out in a carbon coated quartz ampule sealed using a propane-oxygen torch.

Raman spectroscopy was performed using a Horiba/Jobin-Yvon HR800 Raman spectrometer with a 632.8 nm excitation laser wavelength. Spectra on liquid solutions were collected using a quartz cuvette enclosed in a nitrogen atmosphere.

X-ray diffraction analysis was conducted using a Rigaku SmartLab Diffractometer under ambient conditions, employing parallel beam geometry with an incident beam angle of 0.5 degrees. Data collection utilized a Cu Kα source (λ = 1.5406 Å) operated at 40 kV and 44 mA.

Scanning electron microscopy (SEM) and Energy Dispersive X-ray measurements were performed using the FEI Nova three-dimensional system equipped with an Everhart Thornley detector. The measurements were carried out at an accelerating voltage of 10 kV with a working distance of 5 mm. The samples were coated with ~10 nm of platinum for better image resolution.

Reflectance data were obtained employing a PerkinElmer Lambda 950 spectrometer equipped with an integrating sphere.

NMR spectra were recorded on a Bruker AVANCE III 400 MHz spectrometer, and chemical shifts were referenced to residual solvent signals for both ^{1}H. For ^{1}H NMR, the zg30 pulse sequence was utilized with 9 scans, a 1-second relaxation delay, and an acquisition time of 2.1955 seconds.

4.2 Alumina Deposition

A thin layer of alumina was coated onto the glass substrate to improve the surface wettability during the coating process. The alumina also acts as a barrier and prevents cationic diffusion from substrate. Eagle XG glass was thoroughly rinsed with DI water, 2-propanol, and methanol, followed by sonication in an alconox bath and DI water. The substrate was blow dried using a

nitrogen gun. Subsequently, the glass was cleaned in a UV-ozone cleaner for 30 minutes. Commercial alumina nanoparticle solution was diluted by combining 0.2 ml of the commercial solution with 1.8 ml of Isopropanol. The resulting solution was spin-coated onto the cleaned EXG glass at 1000 RPM for 1 minute, followed by annealing at 100 °C for 1 minute and then at 500 °C for 30 minutes.

4.3 Sample preparation

All chemical storage, solution preparation, thin film coating, and sample handling were conducted inside nitrogen- and ultra-high purity (UHP) argon-filled gloveboxes. The ampules were sealed using a Schlenk line with UHP argon as the purging gas. Table 2 summarizes the four different synthesis methods discussed in this work.

Table 2: Synthesis methods discussed in this work.

Method	**Precursors used**	**Powder/thin film**	**Product**
Solid-State Synthesis	$BaS + ZrS_2$ powders	Powders	$BaZrS_3$ and RP phases
Stacked metal sulfides	MS_3 using halide precursors + BaS stack	Thin film	$BaMS_3$ M= Ti, Zr, Hf
Hybrid colloidal Inks	Colloidal MS_3 + BaS using sulfide precursors	Thin film	$BaMS_3$ M= Ti, Zr, Hf
Selenium flux	$BaS + MS_2$ powders with Se	Powders	$BaMS_3$ M= Ti, Zr, Hf

Solid-State Synthesis:

BaS, ZrS_2 and S were loaded into borosilicate ampules in the desired ratios. Before sealing with a butane-air torch, the ampules underwent three cycles of vacuum-argon purging. The heat treatment was performed in a refractory tube furnace at the designated temperature and duration, followed by natural cooling.

The sulfur pressure was calculated at the synthesis temperature using the ideal gas law, with S6 assumed to be the predominant sulfur species. Borosilicate ampules with a nominal volume of 10 ml were used; however, for the calculations, the volume was considered slightly larger to account for the additional volume contributed by the ampule stem.

The synthesized powder was subjected to two rinses with DI water to eliminate water-soluble secondary phases such as BaS_3. The powder was then dried with flowing argon gas.

Stacked metal sulfides method:

Amine-Thiol: A 0.3 M solution of $ZrCl_4$ was prepared with the butylamine: 2-methyl-2-propanethol molar ratio of 1:2.2. 2-methyl-2-propanethiol was added first to the metal precursor, followed by butylamine. The solution was stirred overnight at 35 °C and used for coating.

Amine-CS_2: A 0.3 M solution of $ZrCl_4$ was prepared with a butylamine: CS_2: pyridine molar ratio of 1:1:1. Butylamine was added first to the metal precursor, followed by CS_2 and pyridine. The solution was stirred overnight at 35 °C and used for coating. Similar dissolution procedures were followed for $ZrBr_4$, ZrI_4, $TiCl_4$, and $HfCl_4$.

Amine-Thiourea: A 0.3 M solution of $ZrCl_4$ and 2 M thiourea in butylamine was stirred overnight at 35 °C and used. $ZrCl_4$ and thiourea were mixed together, and butylamine was added.

DMF-Thiourea: A 0.3 M solution of $ZrCl_4$ and 3 M thiourea in dimethylformamide (DMF) was stirred overnight at 35 °C and used. $ZrCl_4$ and thiourea were mixed together, and DMF was added.

Cp^*_2Ba Dissolution: A 0.3 M solution of Cp^*_2Ba was prepared with the butylamine: 2-methyl-2-propanethol molar ratio of 1:1. 2-methyl-2-propanethiol was added first to the metal precursor, followed by butylamine.

Bilayer fabrication: In one route, the four $ZrCl_4$ solutions routes discussed above were coated, annealed, and sulfurized to fabricate the bottom layer of ZrS_3. The samples were sealed in an ampule with HfH_2 and sulfur and heated to 575 °C for 6 h to synthesize the bottom ZrS_3 layer. Cp^*_2Ba was blade coated on top of ZrS_3, sealed in an ampule, and heated at 575 °C for 2 h to

synthesize $BaZrS_3$. Similar procedure was adapted for the iodide and bromide salts as well as $BaHfS_3$ and $BaTiS_3$.

In another route, the $ZrCl_4$-amine-CS_2 ink was coated and annealed on the hotplate at 450 °C for 30 minutes. Cp^*_2Ba was blade coated on top, sealed in an ampule, and heated at 575 °C for 2 h to synthesize $BaZrS_3$.

Hybrid colloidal precursors method:

ZrS_3 powder was synthesized by heating Zr powder with excess sulfur sealed in an ampule at 575 °C for 16 h. A 0.2 M suspension of this ZrS_3 powder was sonicated in pyridine for 2 days to achieve a stable colloidal solution. Simultaneously, a 0.2 M solution of BaS was prepared with propylamine: CS_2: pyridine molar ratio of 1:1:1.5. Propylamine was added first to the metal precursor, followed by CS_2 and pyridine. The solution was stirred for 3-4 days at 35 °C and combined with the ZrS_3 colloidal solution. The solution was then blade-coated, sealed, and sulfurized.

Similar procedures were repeated for Ba-Hf-S and Ba-Ti-S synthesis, with the only difference being the starting precursors. HfH_2 and TiH_2 were used as precursors to synthesize binary sulfides.

Sulfurization:

The following procedure was followed for the thin film deposition in the stacked metal sulfides and hybrid colloidal precursors method.

Solutions were blade-coated using an automated blade coater at a speed of 15 mm per second with a single pass, followed by annealing at 350 °C for 2 minutes on a hot plate and cooling for 1 minute. The coating was repeated 6-8 times on alumina-coated Eagle XG substrates. The resulting films were transferred to a 5ml ampule containing 5 mg of HfH_2 and 15 mg of sulfur. The ampules underwent three purging cycles with vacuum-UHP argon and were sealed using a butane-fueled blowtorch. Subsequently, the ampules were heated in a refractory furnace to the desired temperature and cooled naturally under a slow argon flow.

Selenium Liquid Flux:

The powder synthesis experiments were conducted using borosilicate ampules, which were loaded with either 0.2 mmol BaS, 0.2 mmol ZrS_2, and 30 mg selenium in a 20 ml ampule, or 0.1 mmol BaS, 0.1 mmol ZrS_2, and 15 mg selenium in a 10 ml ampule. Before sealing with a butane-air torch, the ampules underwent three cycles of vacuum-argon purging. The heat treatment was performed in a refractory tube furnace at the designated temperature and duration, followed by natural cooling.

The synthesized $BaMS_3$ (M=Ti, Zr, Hf) powder was subjected to two rinses with DI water to eliminate any water-soluble secondary phases. The water-washed powder was further washed in a 1:5 vol: vol mixture of ethanedithiol-propylamine to wash away any residual selenium. The powder was stirred in amine-thiol solvent overnight at room temperature. The powder was afterward dried with flowing argon gas.

Conflict of Interest

The authors declare no conflict of interest.

Data Availability

The data supporting this article have been included in the Supplementary Information.

Acknowledgments

The authors acknowledge the National Science Foundation's financial support through Grants 1735282-NRT (SFEWS) and 10001536 (INFEWS). Special thanks are extended to Prof. Suzanne C. Bart, Dr. Apurva A. Pradhan, Dr. Jonathan W. Turnley, and Madeleine C. Uible for their valuable discussions regarding the project.

Supplementary Information

Information on additional X-ray diffraction, Raman, EDX, ^{1}H NMR, and liquid Raman data are provided in the supplementary information.

References

(1) Wang, A.; Zuo, C.; Niu, X.; Ding, L.; Ding, J.; Hao, F. Recent Promise of Lead-Free Halide Perovskites in Optoelectronic Applications. *Chemical Engineering Journal* **2023**, *451*, 138926. https://doi.org/10.1016/j.cej.2022.138926.

(2) Hu, H.; Dong, B.; Zhang, W. Low-Toxic Metal Halide Perovskites: Opportunities and Future Challenges. *J Mater Chem A Mater* **2017**, *5* (23), 11436–11449. https://doi.org/10.1039/C7TA00269F.

(3) Kovalenko, M. V.; Protesescu, L.; Bodnarchuk, M. I. Properties and Potential Optoelectronic Applications of Lead Halide Perovskite Nanocrystals. *Science (1979)* **2017**, *358* (6364), 745–750. https://doi.org/10.1126/science.aam7093.

(4) Park, B.; Seok, S. Il. Intrinsic Instability of Inorganic–Organic Hybrid Halide Perovskite Materials. *Advanced Materials* **2019**, *31* (20). https://doi.org/10.1002/adma.201805337.

(5) Feurer, T.; Reinhard, P.; Avancini, E.; Bissig, B.; Löckinger, J.; Fuchs, P.; Carron, R.; Weiss, T. P.; Perrenoud, J.; Stutterheim, S.; Buecheler, S.; Tiwari, A. N. Progress in Thin Film CIGS Photovoltaics – Research and Development, Manufacturing, and Applications. *Progress in Photovoltaics: Research and Applications* **2017**, *25* (7), 645–667. https://doi.org/10.1002/pip.2811.

(6) Giraldo, S.; Jehl, Z.; Placidi, M.; Izquierdo-Roca, V.; Pérez-Rodríguez, A.; Saucedo, E. Progress and Perspectives of Thin Film Kesterite Photovoltaic Technology: A Critical Review. *Advanced Materials* **2019**, *31* (16). https://doi.org/10.1002/adma.201806692.

(7) Theelen, M.; Daume, F. Stability of Cu(In,Ga)Se2 Solar Cells: A Literature Review. *Solar Energy* **2016**, *133*, 586–627. https://doi.org/10.1016/j.solener.2016.04.010.

(8) Sopiha, K. V; Comparotto, C.; Márquez, J. A.; Scragg, J. J. S. Chalcogenide Perovskites: Tantalizing Prospects, Challenging Materials. *Advanced Optical Materials*. December 13, 2022, p 2101704. https://doi.org/10.1002/adom.202101704.

(9) Ju, M.; Dai, J.; Ma, L.; Zeng, X. C. Perovskite Chalcogenides with Optimal Bandgap and Desired Optical Absorption for Photovoltaic Devices. *Adv Energy Mater* **2017**, *7* (18), 1700216. https://doi.org/10.1002/aenm.201700216.

(10) Sun, Y.-Y.; Agiorgousis, M. L.; Zhang, P.; Zhang, S. Chalcogenide Perovskites for Photovoltaics. *Nano Lett* **2015**, *15* (1), 581–585. https://doi.org/10.1021/nl504046x.

(11) Filippone, S.; Zhao, B.; Niu, S.; Koocher, N. Z.; Silevitch, D.; Fina, I.; Rondinelli, J. M.; Ravichandran, J.; Jaramillo, R. Discovery of Highly Polarizable Semiconductors BaZrS3 and Ba3Zr2S7. *Phys Rev Mater* **2020**, *4* (9), 091601. https://doi.org/10.1103/PhysRevMaterials.4.091601.

(12) Wei, X.; Hui, H.; Zhao, C.; Deng, C.; Han, M.; Yu, Z.; Sheng, A.; Roy, P.; Chen, A.; Lin, J.; Watson, D. F.; Sun, Y. Y.; Thomay, T.; Yang, S.; Jia, Q.; Zhang, S.; Zeng, H. Realization of BaZrS3 Chalcogenide Perovskite Thin Films for Optoelectronics. *Nano Energy* **2020**, *68*, 104317. https://doi.org/10.1016/j.nanoen.2019.104317.

(13) Hanzawa, K.; Iimura, S.; Hiramatsu, H.; Hosono, H. Material Design of Green-Light-Emitting Semiconductors: Perovskite-Type Sulfide SrHfS3. *J Am Chem Soc* **2019**, *141* (13), 5343–5349. https://doi.org/10.1021/jacs.8b13622.

(14) Liang, Y.; Li, J.; Chen, Z.; Li, G.; Li, M.; Jia, M.; Chen, X.; Li, X.; Han, Y.; Shi, Z. Tapping the Light Emitting Potential of Chalcogenide Perovskite $SrHfS_3$ via Eu^{2+} Doping. *Adv Opt Mater* **2024**, *12* (6). https://doi.org/10.1002/adom.202301977.

(15) Han, Y.; Fang, J.; Liang, Y.; Gao, H.; Yang, J.; Chen, X.; Yuan, Y.; Shi, Z. Preparation of Chalcogenide Perovskite SrHfS3 and Luminescent SrHfS3:Eu2+ Thin Films. *Appl Phys Lett* **2024**, *124* (13). https://doi.org/10.1063/5.0200555.

(16) Ishii, M.; Saeki, M. Raman and Infrared Spectra of BaTiS3 and BaNbS3. *physica status solidi (b)* **1992**, *170* (1), K49–K54. https://doi.org/10.1002/pssb.2221700149.

(17) Paudel, T. R.; Tsymbal, E. Y. Evaluating the Thermoelectric Properties of BaTiS3 by Density Functional Theory. *ACS Omega* **2020**, *5* (21), 12385–12390. https://doi.org/10.1021/acsomega.0c01139.

(18) Comparotto, C.; Davydova, A.; Ericson, T.; Riekehr, L.; Moro, M. V.; Kubart, T.; Scragg, J. Chalcogenide Perovskite BaZrS3: Thin Film Growth by Sputtering and Rapid Thermal Processing. *ACS Appl Energy Mater* **2020**, *3* (3), 2762–2770. https://doi.org/10.1021/acsaem.9b02428.

(19) Sharma, S.; Ward, Z.; Bhimani, K.; Li, K.; Lakhnot, A.; Jain, R.; Shi, S.-F.; Terrones, H.; Koratkar, N. Bandgap Tuning in BaZrS3 Perovskite Thin Films. *ACS Appl Electron Mater* **2021**, *3* (8), 3306–3312. https://doi.org/10.1021/acsaelm.1c00575.

(20) Sadeghi, I.; Ye, K.; Xu, M.; Li, Y.; LeBeau, J. M.; Jaramillo, R. Making BaZrS3 Chalcogenide Perovskite Thin Films by Molecular Beam Epitaxy. *Adv Funct Mater* **2021**, *31* (45), 2105563. https://doi.org/10.1002/adfm.202105563.

(21) Márquez, J. A.; Rusu, M.; Hempel, H.; Ahmet, I. Y.; Kölbach, M.; Simsek, I.; Choubrac, L.; Gurieva, G.; Gunder, R.; Schorr, S.; Unold, T. BaZrS3 Chalcogenide Perovskite Thin Films by H2S Sulfurization of Oxide Precursors. *J Phys Chem Lett* **2021**, *12* (8), 2148–2153. https://doi.org/10.1021/acs.jpclett.1c00177.

(22) Wang, Y.; Sato, N.; Fujino, T. Synthesis of BaZrS3 by Short Time Reaction at Lower Temperatures. *J Alloys Compd* **2001**, *327* (1–2), 104–112. https://doi.org/10.1016/S0925-8388(01)01553-5.

(23) Bystrický, R.; Tiwari, S. K.; Hutár, P.; Vančo, L.; Sýkora, M. Synthesis of Sulfide Perovskites by Sulfurization with Boron Sulfides. *Inorg Chem* **2022**. https://doi.org/10.1021/acs.inorgchem.2c03200.

(24) Niu, S.; Milam-Guerrero, J.; Zhou, Y.; Ye, K.; Zhao, B.; Melot, B. C.; Ravichandran, J. Thermal Stability Study of Transition Metal Perovskite Sulfides. *J Mater Res* **2018**, *33* (24), 4135–4143. https://doi.org/10.1557/jmr.2018.419.

(25) Niu, S.; Zhao, B.; Ye, K.; Bianco, E.; Zhou, J.; McConney, M. E.; Settens, C.; Haiges, R.; Jaramillo, R.; Ravichandran, J. Crystal Growth and Structural Analysis of Perovskite Chalcogenide BaZrS 3 and Ruddlesden–Popper Phase Ba3Zr2S7. *J Mater Res* **2019**, *34* (22), 3819–3826. https://doi.org/10.1557/jmr.2019.348.

(26) Comparotto, C.; Ström, P.; Donzel-Gargand, O.; Kubart, T.; Scragg, J. J. S. Synthesis of BaZrS3 Perovskite Thin Films at a Moderate Temperature on Conductive Substrates. *ACS Appl Energy Mater* **2022**, *5* (5), 6335–6343. https://doi.org/10.1021/acsaem.2c00704.

(27) Vincent, K. C.; Agarwal, S.; Turnley, J. W.; Agrawal, R. Liquid Flux–Assisted Mechanism for Modest Temperature Synthesis of Large-Grain BaZrS3 and BaHfS3 Chalcogenide Perovskites. *Advanced Energy and Sustainability Research* **2023**, *2300010*, 2300010. https://doi.org/10.1002/aesr.202300010.

(28) Yang, R.; Jess, A. D.; Fai, C.; Hages, C. J. Low-Temperature, Solution-Based Synthesis of Luminescent Chalcogenide Perovskite BaZrS3 Nanoparticles. *J Am Chem Soc* **2022**, *144* (35), 15928–15931. https://doi.org/10.1021/jacs.2c06168.

(29) Yang, R.; Nelson, J.; Fai, C.; Yetkin, H. A.; Werner, C.; Tervil, M.; Jess, A. D.; Dale, P. J.; Hages, C. J. A Low-Temperature Growth Mechanism for Chalcogenide Perovskites. *Chemistry of Materials* **2023**, *35* (12), 4743–4750. https://doi.org/10.1021/acs.chemmater.3c00494.

(30) Pradhan, A. A.; Uible, M. C.; Agarwal, S.; Turnley, J. W.; Khandelwal, S.; Peterson, J. M.; Blach, D. D.; Swope, R. N.; Huang, L.; Bart, S. C.; Agrawal, R. Synthesis of BaZrS3 and BaHfS3 Chalcogenide Perovskite Films Using Single-Phase Molecular Precursors at Moderate Temperatures. *Angewandte Chemie International Edition* **2023**. https://doi.org/10.1002/anie.202301049.

(31) Turnley, J. W.; Vincent, K. C.; Pradhan, A. A.; Panicker, I.; Swope, R.; Uible, M. C.; Bart, S. C.; Agrawal, R. Solution Deposition for Chalcogenide Perovskites: A Low-Temperature Route to BaMS3 Materials (M = Ti, Zr, Hf). *J Am Chem Soc* **2022**, *144* (40), 18234–18239. https://doi.org/10.1021/jacs.2c06985.

(32) Murria, P.; Miskin, C. K.; Boyne, R.; Cain, L. T.; Yerabolu, R.; Zhang, R.; Wegener, E. C.; Miller, J. T.; Kenttämaa, H. I.; Agrawal, R. Speciation of CuCl and CuCl2 Thiol-Amine Solutions and Characterization of Resulting Films: Implications for Semiconductor Device Fabrication. *Inorg Chem* **2017**, *56* (23), 14396–14407. https://doi.org/10.1021/acs.inorgchem.7b01359.

(33) Clark, J. A.; Murray, A.; Lee, J.; Autrey, T. S.; Collord, A. D.; Hillhouse, H. W. Complexation Chemistry in N,N -Dimethylformamide-Based Molecular Inks for Chalcogenide Semiconductors and Photovoltaic Devices. *J Am Chem Soc* **2019**, *141* (1), 298–308. https://doi.org/10.1021/jacs.8b09966.

(34) Suresh, S.; Uhl, A. R. Present Status of Solution-Processing Routes for Cu(In,Ga)(S,Se)2 Solar Cell Absorbers. *Adv Energy Mater* **2021**, *11* (14), 2003743. https://doi.org/10.1002/aenm.202003743.

(35) Turnley, J. W.; Agrawal, R. Solution Processed Metal Chalcogenide Semiconductors for Inorganic Thin Film Photovoltaics. *Chemical Communications* **2024**, *60* (40), 5245–5269. https://doi.org/10.1039/D4CC01057D.

(36) Kepp, K. P. A Quantitative Scale of Oxophilicity and Thiophilicity. *Inorg Chem* **2016**, *55* (18), 9461–9470. https://doi.org/10.1021/acs.inorgchem.6b01702.

(37) Zilevu, D.; Creutz, S. E. Solution-Phase Synthesis of Group 3–5 Transition Metal Chalcogenide Inorganic Nanomaterials. *Chemical Communications* **2023**, *59* (57), 8779–8798. https://doi.org/10.1039/D3CC01731A.

(38) Agarwal, S.; Turnley, J. W.; Pradhan, A. A.; Agrawal, R. Moderate Temperature Sulfurization and Selenization of Highly Stable Metal Oxides: An Opportunity for Chalcogenide Perovskites. *J Mater Chem C Mater* **2023**, *11* (45), 15817–15823. https://doi.org/10.1039/D3TC02716C.

(39) Gurieva, G.; Ferreira, R.; Knoll, P.; Schorr, S. $Cu_2ZnSnSe_4$: How Far Does Off-Stoichiometry Go? *physica status solidi (a)* **2018**, *215* (17). https://doi.org/10.1002/pssa.201700957.

(40) Sopiha, K. V.; Larsen, J. K.; Keller, J.; Edoff, M.; Platzer-Björkman, C.; Scragg, J. J. S. Off-Stoichiometry in I–III–VI $_2$ Chalcopyrite Absorbers: A Comparative Analysis of Structures and Stabilities. *Faraday Discuss* **2022**, *239*, 357–374. https://doi.org/10.1039/D2FD00105E.

(41) Monsefi, M.; Kuo, D.-H. Defect State and Electric Transport of the Cu-Poor, Cu-Rich, and In-Rich Cu(In,Ga)Se2 Bulk Materials. *Mater Chem Phys* **2014**, *145* (1–2), 255–259. https://doi.org/10.1016/j.matchemphys.2014.02.019.

(42) Nakamura, M.; Yamaguchi, K.; Kimoto, Y.; Yasaki, Y.; Kato, T.; Sugimoto, H. Cd-Free $Cu(In,Ga)(Se,S)_2$ Thin-Film Solar Cell With Record Efficiency of 23.35%. *IEEE J Photovolt* **2019**, *9* (6), 1863–1867. https://doi.org/10.1109/JPHOTOV.2019.2937218.

(43) Wu, X.; Gao, W.; Chai, J.; Ming, C.; Chen, M.; Zeng, H.; Zhang, P.; Zhang, S.; Sun, Y.-Y. Defect Tolerance in Chalcogenide Perovskite Photovoltaic Material BaZrS3. *Sci China Mater* **2021**, *64* (12), 2976–2986. https://doi.org/10.1007/s40843-021-1683-0.

(44) Meng, W.; Saparov, B.; Hong, F.; Wang, J.; Mitzi, D. B.; Yan, Y. Alloying and Defect Control within Chalcogenide Perovskites for Optimized Photovoltaic Application. *Chemistry of Materials* **2016**, *28* (3), 821–829. https://doi.org/10.1021/acs.chemmater.5b04213.

(45) Han, Y.; Xu, J.; Liang, Y.; Chen, X.; Jia, M.; Zhang, J.; Lian, L.; Liu, Y.; Li, X.; Shi, Z. P-Type Conductive BaZrS3 Thin Film and Its Band Gap Tunning via Ruddlesden-Popper Ba3Zr2S7 and Titanium Alloying. *Chemical Engineering Journal* **2023**, *473*, 145351. https://doi.org/10.1016/j.cej.2023.145351.

(46) Kayastha, P.; Tiwari, D.; Holland, A.; Hutter, O. S.; Durose, K.; Whalley, L. D.; Longo, G. High-Temperature Equilibrium of 3D and 2D Chalcogenide Perovskites. *Solar RRL* **2023**, *7* (9). https://doi.org/10.1002/solr.202201078.

(47) Li, W.; Niu, S.; Zhao, B.; Haiges, R.; Zhang, Z.; Ravichandran, J.; Janotti, A. Band Gap Evolution in Ruddlesden-Popper Phases. *Phys Rev Mater* **2019**, *3* (10), 101601. https://doi.org/10.1103/PhysRevMaterials.3.101601.

(48) Agarwal, S.; Weideman, K.; Rokke, D.; Vincent, K. C.; Zemlyanov, D.; Agrawal, R. Enhancing the Optoelectronic Properties of Solution-Processed $AgInSe_2$ Thin Films for Application in Photovoltaics. *J Mater Chem C Mater* **2024**, *12* (1), 325–336. https://doi.org/10.1039/D3TC03540A.

(49) Larsen, E. M. Zirconium and Hafnium Chemistry. In *Advances in Inorganic Chemistry and Radiochemistry*; 1970; Vol. 13, pp 1–133. https://doi.org/10.1016/S0065-2792(08)60335-0.

(50) Mitzi, D. B.; Yuan, M.; Liu, W.; Kellock, A. J.; Chey, S. J.; Gignac, L.; Schrott, A. G. Hydrazine-Based Deposition Route for Device-Quality CIGS Films. *Thin Solid Films* **2009**, *517* (7), 2158–2162. https://doi.org/10.1016/j.tsf.2008.10.079.

(51) Zhao, X.; Deshmukh, S. D.; Rokke, D. J.; Zhang, G.; Wu, Z.; Miller, J. T.; Agrawal, R. Investigating Chemistry of Metal Dissolution in Amine−Thiol Mixtures and Exploiting It toward Benign Ink Formulation for Metal Chalcogenide Thin Films. *Chem. Mater* **2019**, *31* (15), 5674–5682. https://doi.org/10.1021/acs.chemmater.9b01566.

(52) McCarthy, C. L.; Brutchey, R. L. Solution Deposited $Cu_2BaSnS_{4-x}Se_x$ from a Thiol–Amine Solvent Mixture. *Chemistry of Materials* **2018**, *30* (2), 304–308. https://doi.org/10.1021/acs.chemmater.7b03931.

(53) Teymur, B.; Zhou, Y.; Ngaboyamahina, E.; Glass, J. T.; Mitzi, D. B. Solution-Processed Earth-Abundant $Cu_2BaSn(S,Se)_4$ Solar Absorber Using a Low-Toxicity Solvent. *Chemistry of Materials* **2018**, *30* (17), 6116–6123. https://doi.org/10.1021/acs.chemmater.8b02556.

(54) Shin, D.; Zhu, T.; Huang, X.; Gunawan, O.; Blum, V.; Mitzi, D. B. Earth-Abundant Chalcogenide Photovoltaic Devices with over 5% Efficiency Based on a $Cu_2BaSn(S,Se)_4$ Absorber. *Advanced Materials* **2017**, *29* (24). https://doi.org/10.1002/adma.201606945.

(55) McLeod, S.; Alruqobah, E.; Agrawal, R. Liquid Assisted Grain Growth in Solution Processed Cu(In,Ga)(S,Se)2. *Solar Energy Materials and Solar Cells* **2019**, *195*, 12–23. https://doi.org/10.1016/j.solmat.2019.02.020.

(56) Hages, C. J.; Koeper, M. J.; Miskin, C. K.; Brew, K. W.; Agrawal, R. Controlled Grain Growth for High Performance Nanoparticle-Based Kesterite Solar Cells. *Chemistry of Materials* **2016**, *28* (21), 7703–7714. https://doi.org/10.1021/acs.chemmater.6b02733.

(57) Sashital, S. R.; Gentile, A. L. Liquid Phase Epitaxial Growth of AgGaS2 Using Chalcogenide (Sulphide) Fluxes. *J Cryst Growth* **1984**, *69* (2–3), 379–387. https://doi.org/10.1016/0022-0248(84)90346-4.

(58) Turnley, J. W.; Deshmukh, S. D.; Boulos, V. M.; Spilker, R.; Breckner, C. J.; Ng, K.; Liu, J. K.-Y.; Miller, J. T.; Kenttämaa, H. I.; Agrawal, R. A Selenium-Based "Alkahest": Reactive Dissolutions of Metals and Metal Compounds with *n* -Alkylammonium Polyselenide Solutions. *Inorg Chem Front* **2023**, *10* (20), 6032–6044. https://doi.org/10.1039/D3QI01632C.

(59) Newman, P. J.; MacFarlane, D. R. Preparation of CdSe Quantum Dots in Ionic Liquids. *Zeitschrift für Physikalische Chemie* **2006**, *220* (10), 1473–1481. https://doi.org/10.1524/zpch.2006.220.10.1473.

Supplementary Information

Expanding the Horizons for Viable Precursors and Liquid Fluxes for the Synthesis of $BaZrS_3$ and Related Compounds

Kiruba Catherine Vincent[*, a], Shubhanshu Agarwal[*, a], Zirui Fan[a], Alison Sofia Mesa Canizales[b], and Rakesh Agrawal[**, a]

[a]Davidson School of Chemical Engineering, Purdue University, West Lafayette, IN 47907(USA)
[b]Chemical and Environmental Engineering, Universidad Nacional de Colombia, Bogota D.C. (Colombia)

*Equal Contribution
**Corresponding author: Dr. Rakesh Agrawal. E-mail: agrawalr@purdue.edu

Ba-Zr-S powder reactions

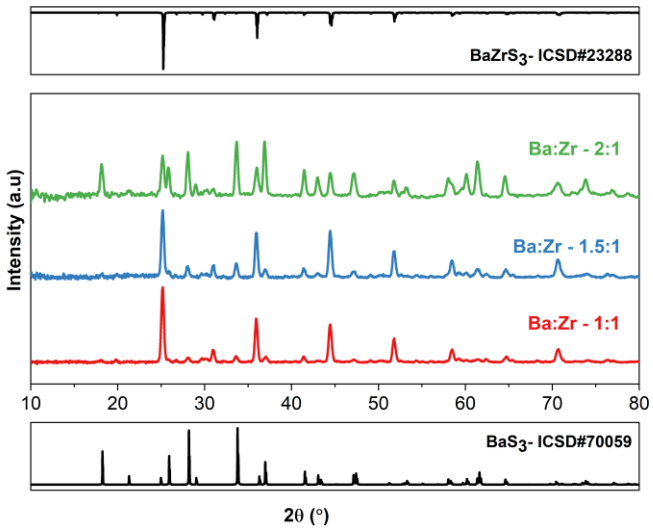

Figure S1. X-ray diffraction pattern of Ba-Zr-S powder synthesized with different Ba:Zr ratios at 575 °C for 12 h with a sulfur pressure of 0.79 atm. BaS and ZrS_2 were used as barium and zirconium precursors, respectively. The X-ray diffraction patterns were collected before rinsing the powders with water as against data in Figure 1.a.

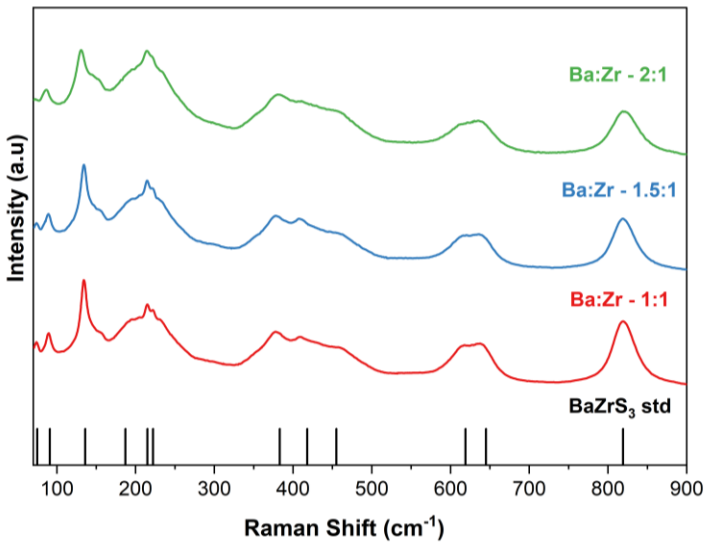

Figure S2. Raman spectra of Ba-Zr-S powder synthesized with different Ba:Zr ratios at 575 °C for 12 h with a sulfur pressure of 0.79 atm. The synthesized powder was washed with water to remove water-soluble impurities (BaS_3). BaS and ZrS_2 were used as barium and zirconium precursors, respectively.

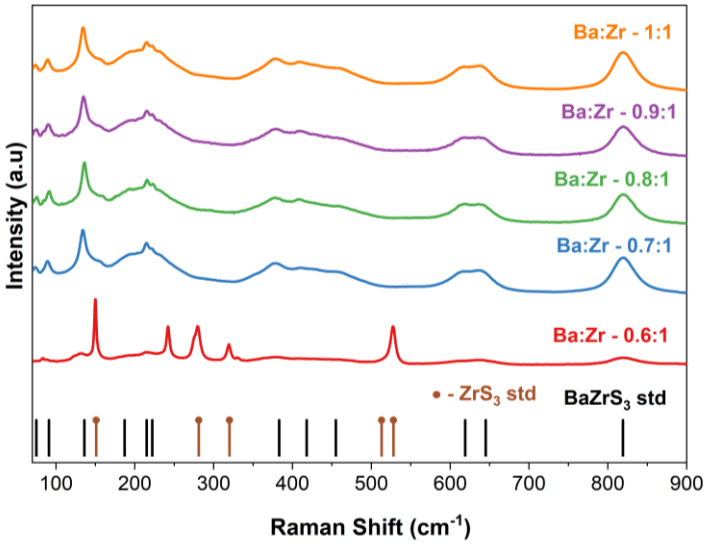

Figure S3. Raman spectra of Ba-Zr-S powder synthesized with different Ba:Zr ratios at 575 °C for 12 h with a sulfur pressure of 0.79 atm. BaS and ZrS_2 were used as barium and zirconium precursors, respectively.

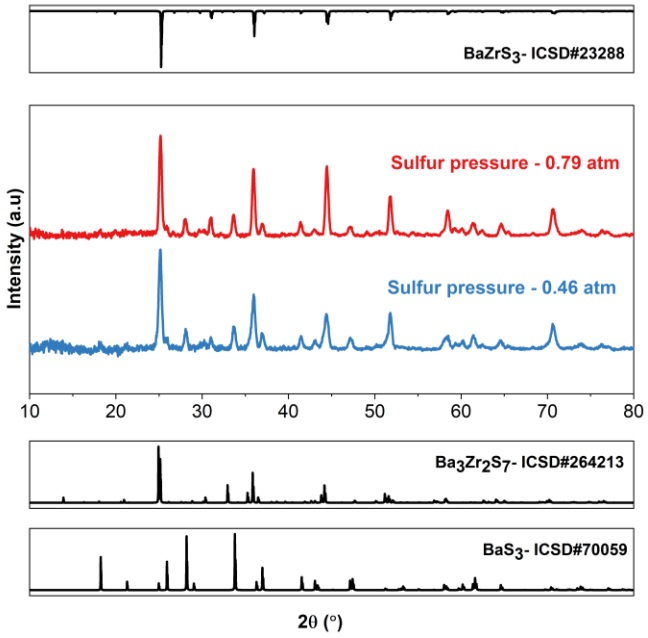

Figure S4. X-ray diffraction pattern of Ba-Zr-S powder synthesized with a Ba:Zr ratio of 1.5:1 and sulfur pressures of 0.79 atm and 0.46 atm, respectively, at 575 °C for 12 h. BaS and ZrS_2 were used as barium and zirconium precursors, respectively.

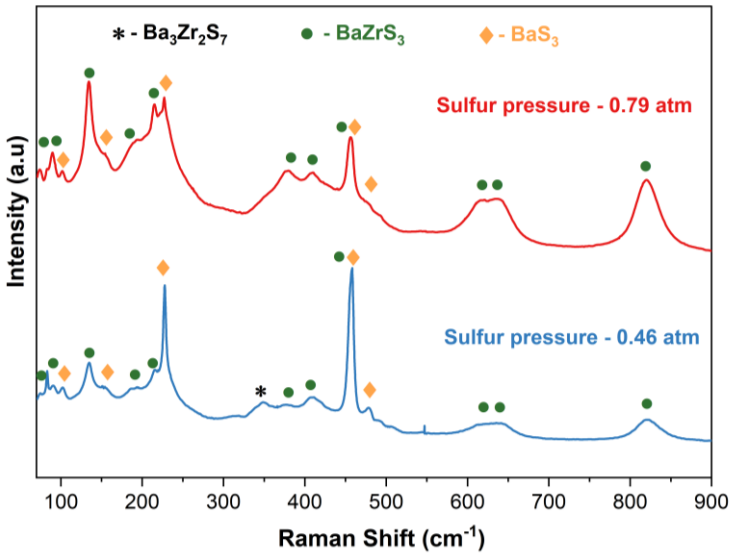

Figure S5. Raman spectra of Ba-Zr-S powder synthesized with a Ba:Zr ratio of 1.5:1 and sulfur pressures of 0.79 atm and 0.46 atm, respectively, at 575 °C for 12 h. BaS and ZrS_2 were used as barium and zirconium precursors, respectively.

Stacked binary metal sulfides

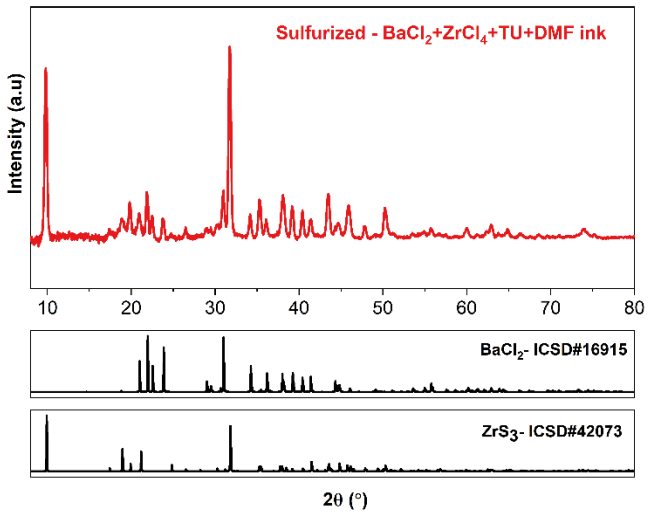

Figure S6. X-ray diffraction analysis confirmed the formation of $BaCl_2$ and ZrS_3 after sulfurizing the as-annealed film obtained from the mixed precursor ink of $BaCl_2$-$ZrCl_4$-thiourea (TU)-dimethyl formamide (DMF). The film underwent sulfurization at 575 °C for 12 h.

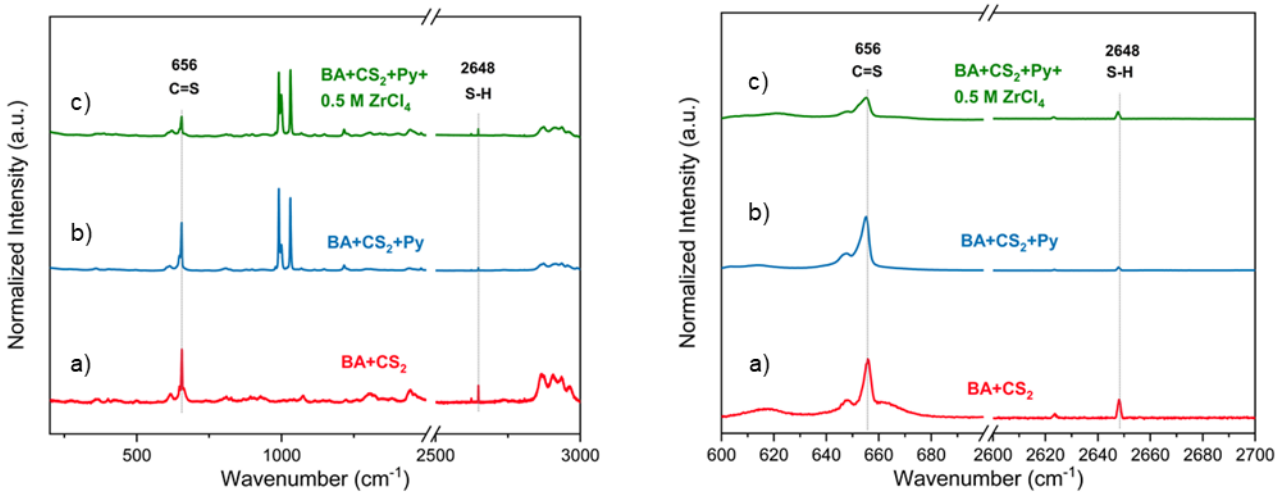

Figure S7. Liquid Raman on a) Butylamine (BA)+CS_2, b) BA+CS_2+Pyridine (Py), and c) BA+CS_2+Py+$ZrCl_4$ (0.5 M). The emergence of a new peak at 2648 cm^{-1} suggests the formation of the dithiocarbamate group. The broadening of the C=S peak at 656 cm^{-1} in (c) indicate metal-sulfur interaction.

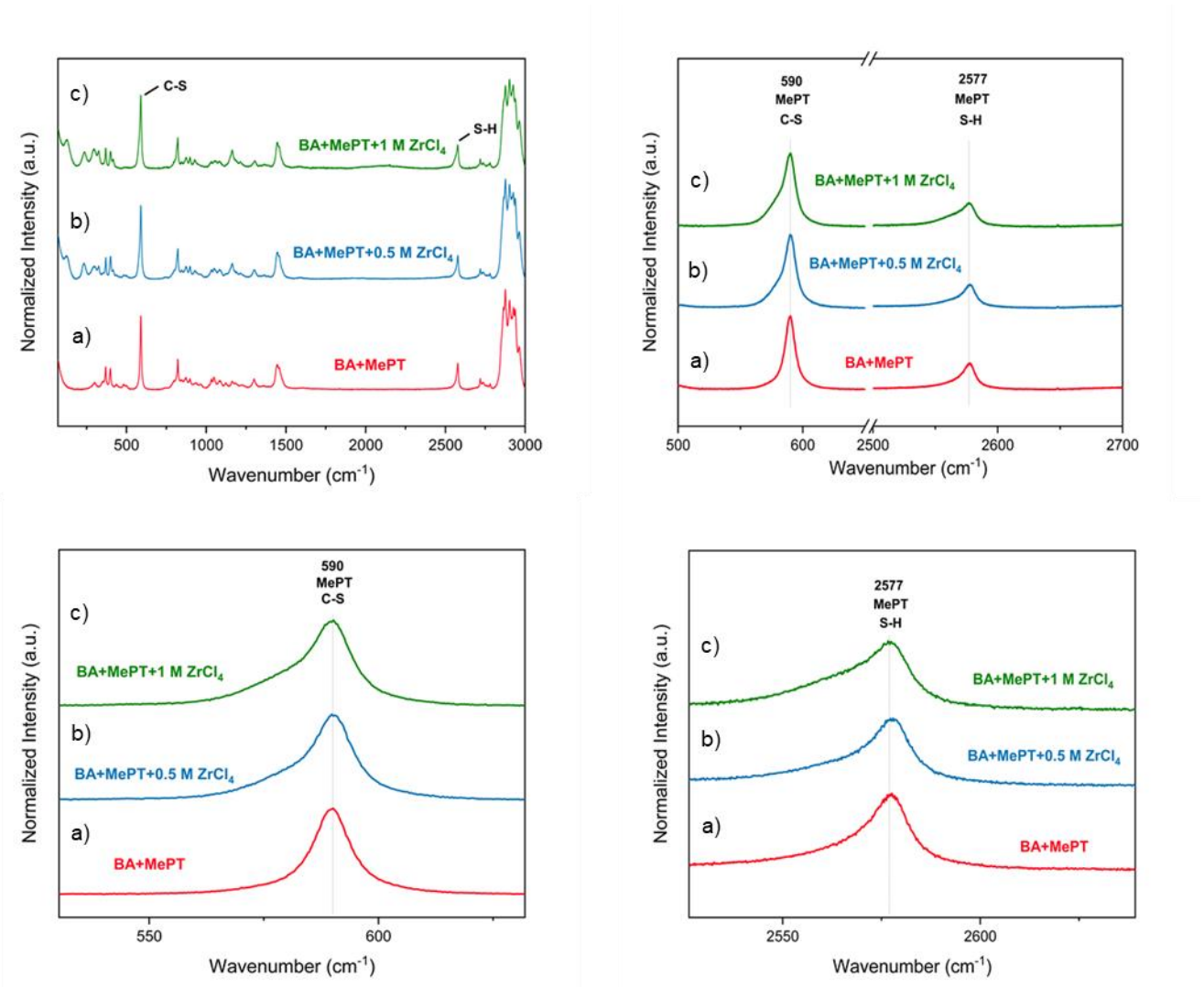

Figure S8. Liquid Raman on Butylamine a) (BA)+2-methyl-2-propanethiol (MePT), b) BA+MePT+$ZrCl_4$ (0.5 M), and c) BA+MePT+$ZrCl_4$ (1 M). The slight broadening and reduction in the ratio of area under peaks of SH to C-S from 0.62 to 0.49 suggests the interaction of metal, sulfur, and thiolate formation. However, insufficient SH peak intensity reduction means the complete substitution of chlorine with thiolate did not occur.

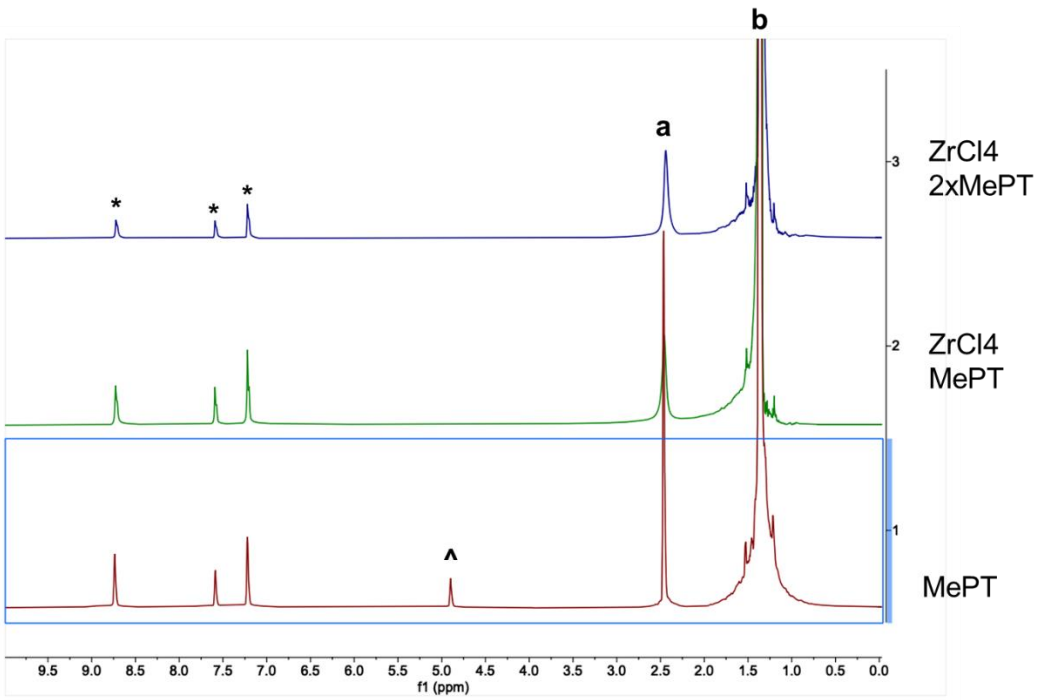

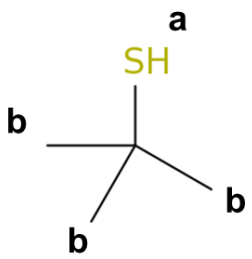

^ water

* d-pyridine

Figure S9. ^{1}H-NMR analysis on only 2-methyl-2-propanethiol (MePT), stoichiometric MePT+$ZrCl_4$, and twice stoichiometric MePT+$ZrCl_4$ in d-pyridine. The slight broadening of the peak for H bound to sulfur suggests the interaction of metal and sulfur and thiolate formation. However, insufficient SH peak intensity reduction means that complete substitution of chlorine with thiolate did not occur.

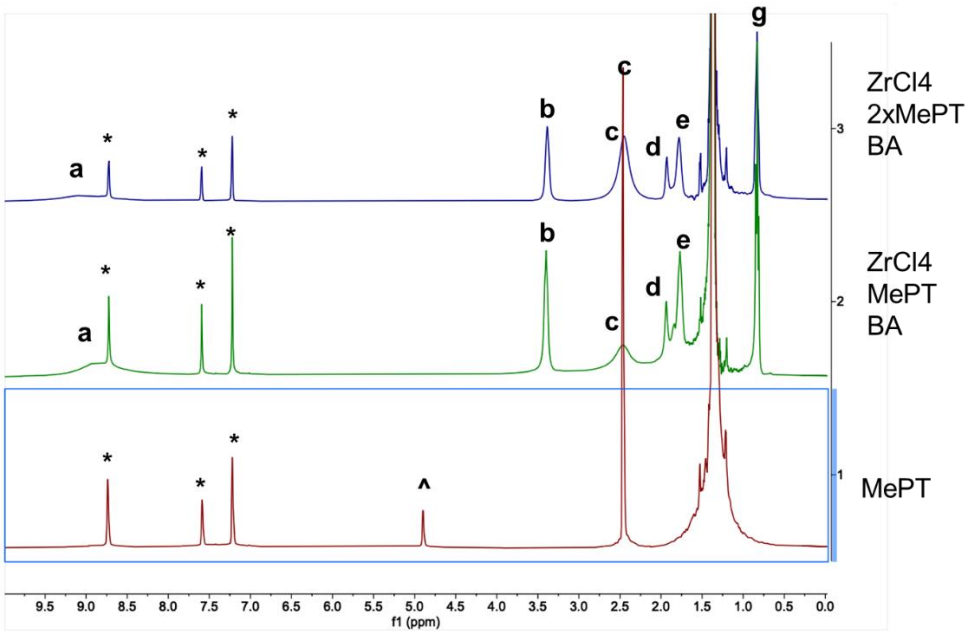

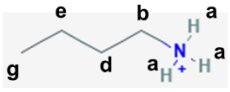

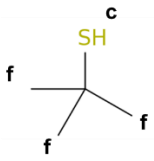

^ water

* d-pyridine

Figure S10. ^{1}H-NMR analysis on only 2-methyl-2-propanethiol (MePT), stoichiometric MePT+ stoichiometric butylamine (BA)+$ZrCl_4$, and twice stoichiometric MePT+stoichiometric BA+$ZrCl_4$ in d-pyridine. The broadening of the peak for proton bound to sulfur and reduction in the ratio of the peak intensities of proton at a-site to proton at b-site suggests the increased interaction of thiol and Butylamine as such intensity reduction was not observed without Butylamine.

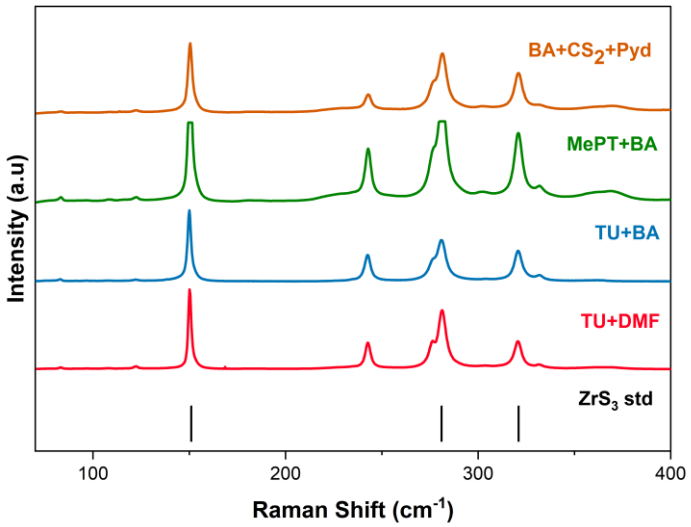

Figure S11. Raman of ZrS_3 film synthesized from 4 different solution chemistries with $ZrCl_4$ metal precursor. The films were sulfurized at 575 °C for 6 h. Reference Raman peaks were identified by Osada et al.[2]

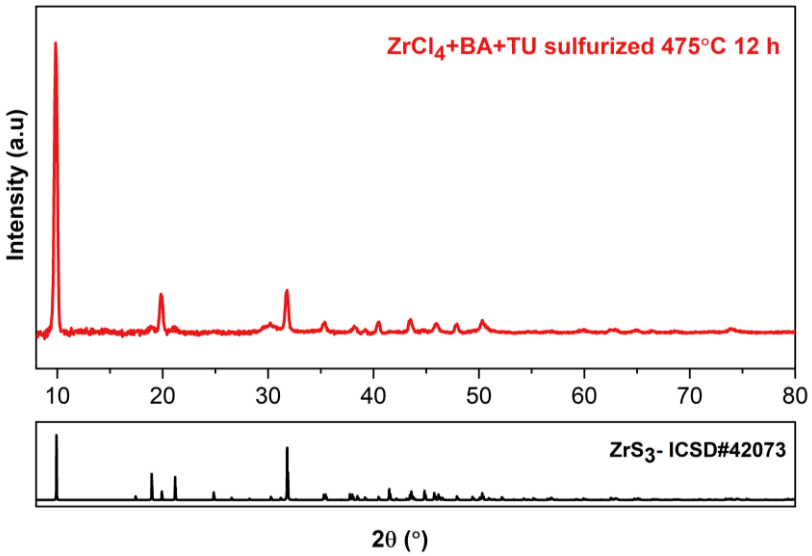

Figure S12. X-ray diffraction pattern of ZrS_3 film synthesized from $ZrCl_4$ precursors. The films were sulfurized at 475 °C for 12 h.

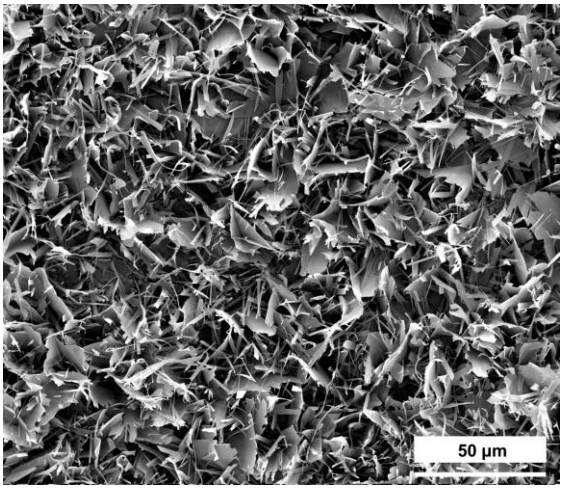

Figure S13. SEM top view of ZrS_3 film synthesized from $ZrCl_4$-2-methyl-2-propanethiol-butylamine solution chemistry. The film was sulfurized at 575 °C for 6 h.

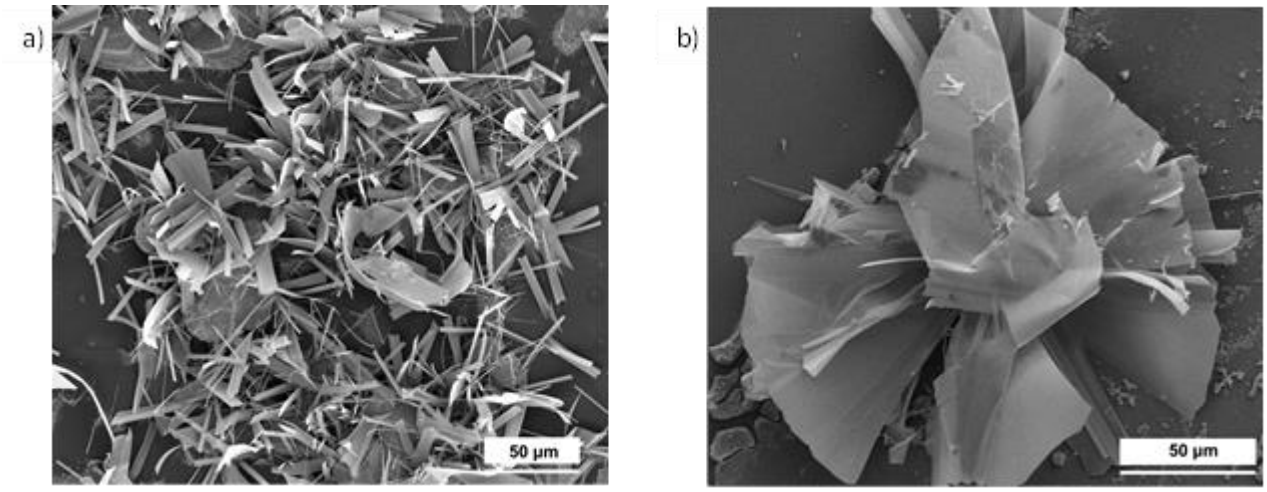

Figure S14. SEM top view of ZrS_3 films synthesized from a) $ZrCl_4$-thiourea-dimethyl formamide solution chemistry and b) $ZrCl_4$-thiourea-butylamine solution chemistry. The films were sulfurized at 575 °C for 6 h.

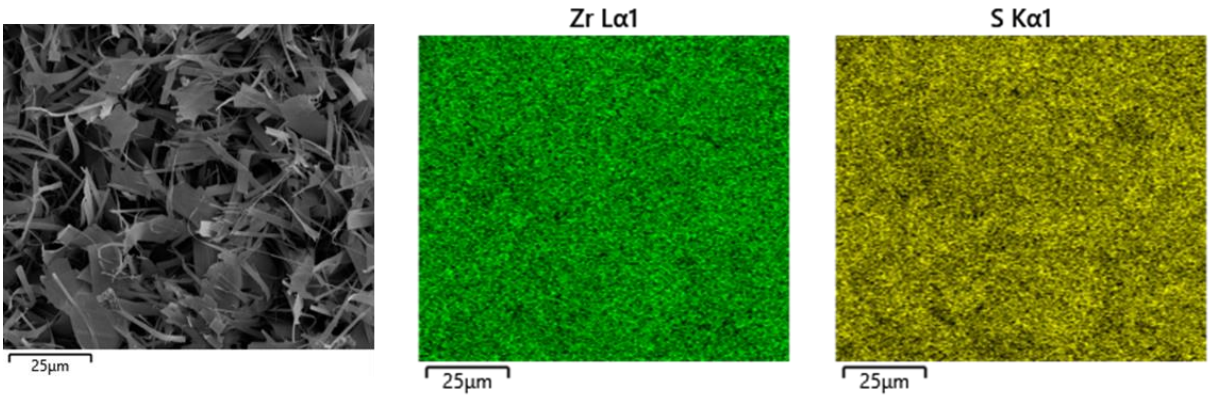

Figure 15. EDX mapping of ZrS_3 film synthesized from $ZrCl_4$-butylamine-CS_2-pyridine solution chemistry confirms only Zr and S in the ZrS_3 grains. The film was sulfurized at 575 °C for 6 h.

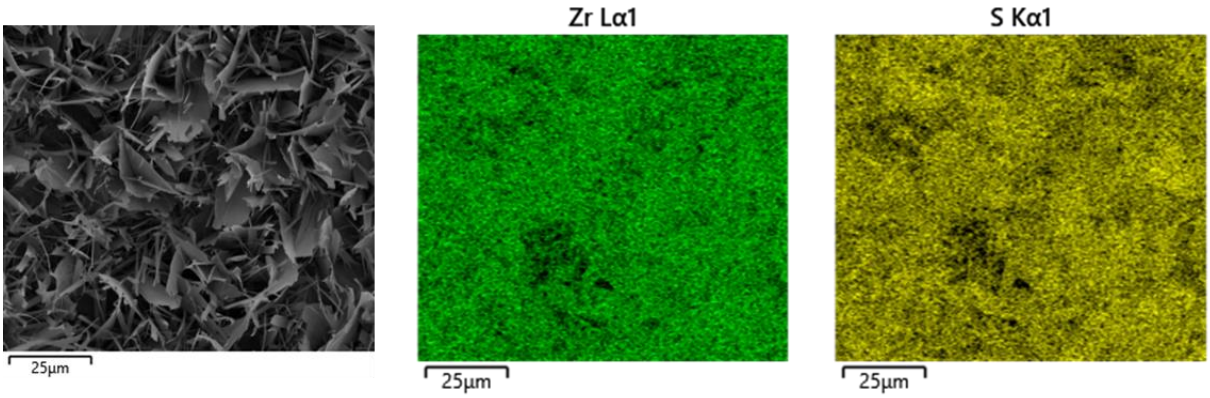

Figure S16. EDX mapping of ZrS_3 film synthesized from $ZrCl_4$-2-methyl-2-propanethiol-butylamine solution chemistry confirms the presence of only Zr and S in the ZrS_3 grains. The film was sulfurized at 575 °C for 6 h.

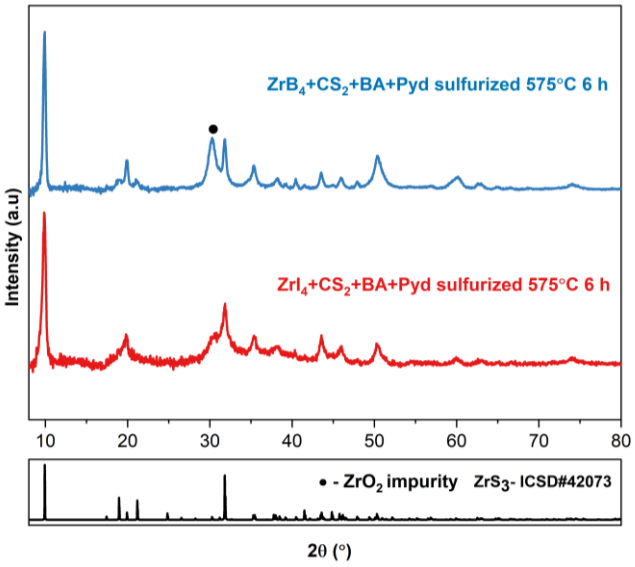

Figure S17. X-ray diffraction pattern of ZrS_3 film synthesized from $ZrBr_4$ and ZrI_4 metal precursors. The films were sulfurized at 575 °C for 6 h.

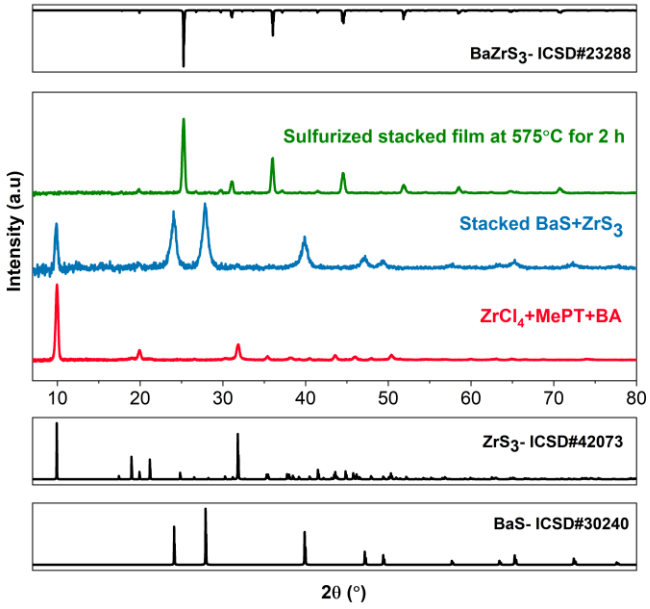

Figure S18. X-ray diffraction pattern of ZrS_3, as-coated bilayer stack of ZrS_3 and BaS, and $BaZrS_3$ after sulfurization where ZrS_3 is synthesized from $ZrCl_4$-2-methyl-2-propanethiol-butylamine solution chemistry. The stacked film was sulfurized at 575 °C for 2 h.

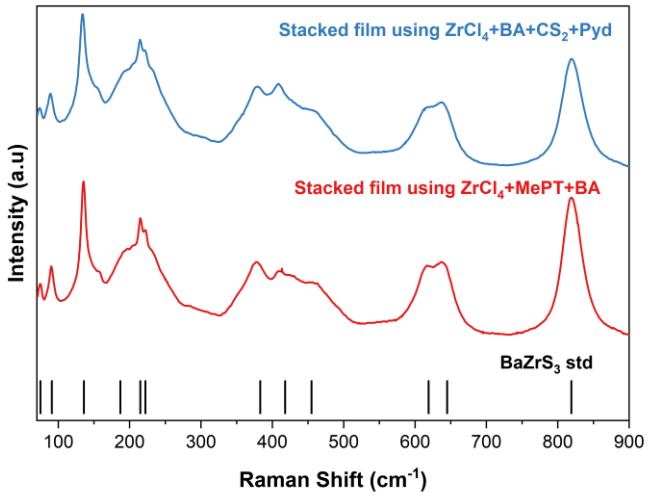

Figure S19. Raman spectra of $BaZrS_3$ films synthesized from the BaS-ZrS_3 stacked film. ZrS_3 layer was achieved through the sulfurization of as-annealed film $ZrCl_4$ solution chemistries. The films were sulfurized at 575 °C for 6 h. Reference Raman peaks were identified by Pandey et al.[1]

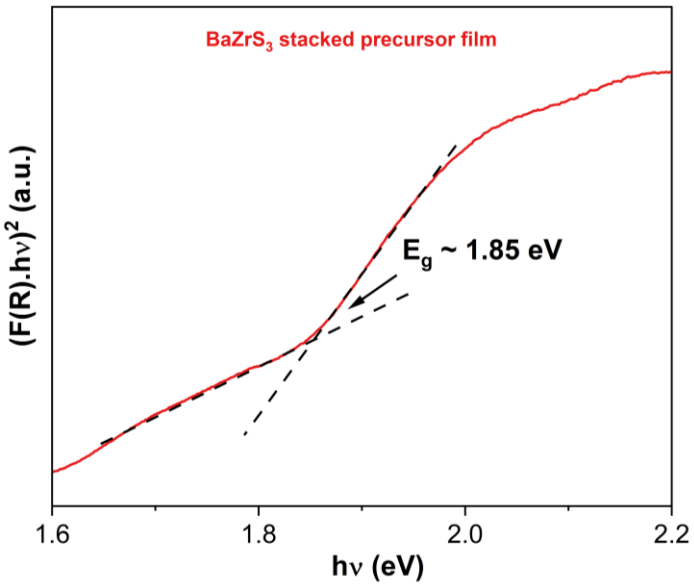

Figure S20. Kubelka-Munk transformation applied to the diffuse reflectance spectra of the $BaZrS_3$ film derived from stacked BaS-ZrS_3 precursor film. The stacked film was sulfurized at 575 °C for 2 h.

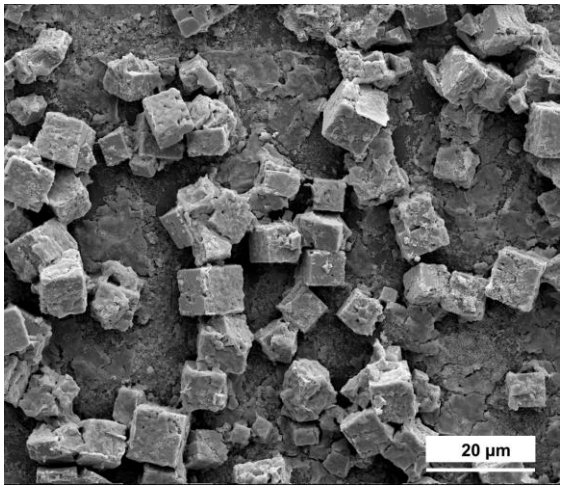

Figure S21. SEM top view of $BaZrS_3$ after sulfurization of ZrS_3-BaS stack where ZrS_3 is synthesized from $ZrCl_4$-2-methyl-2-propanethiol-butylamine. The film was sulfurized at 575 °C for 2 h.

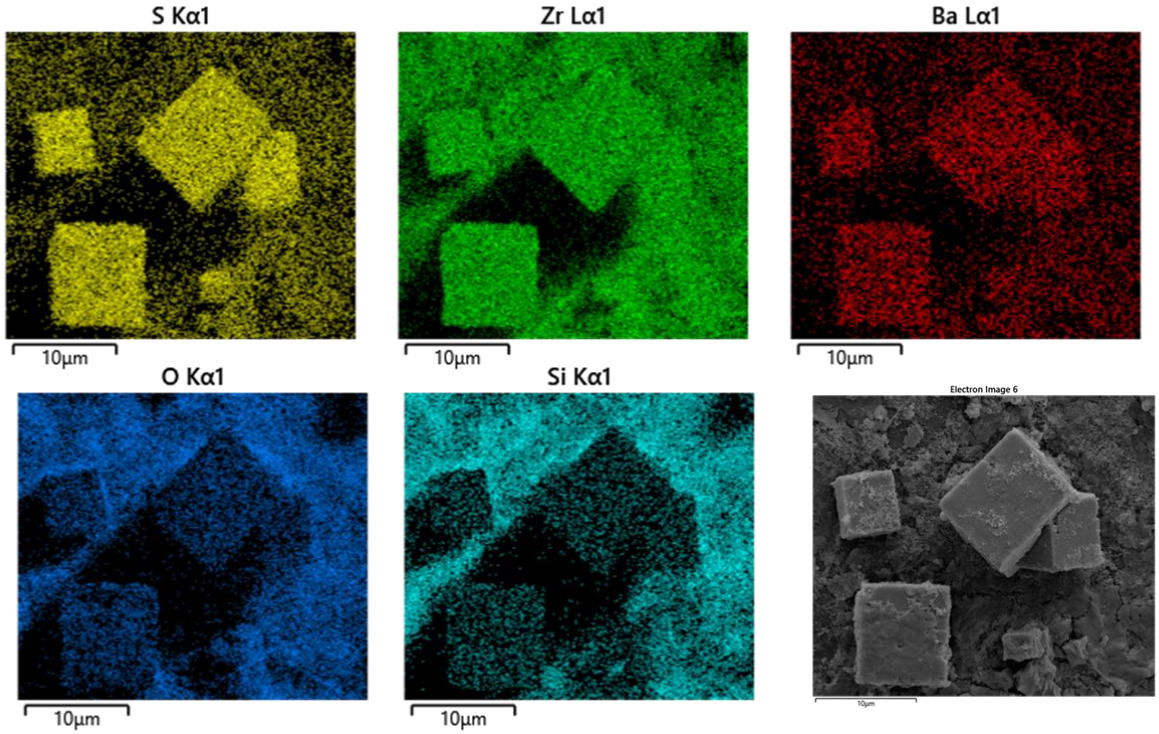

Figure S22. EDX map of $BaZrS_3$ after sulfurization of ZrS_3-BaS stack where ZrS_3 is synthesized from $ZrCl_4$-2-methyl-2-propanethiol-butylamine. The film was sulfurized at 575 °C for 2 h.

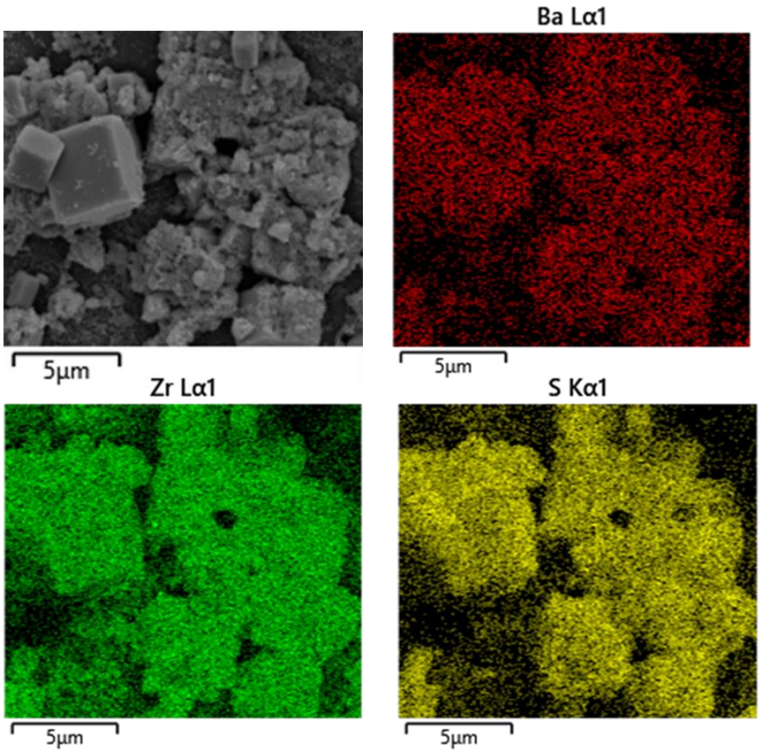

Figure S23. EDX map of $BaZrS_3$ after sulfurization of ZrS_3-BaS stack where ZrS_3 is synthesized from $ZrCl_4$-CS_2- butylamine-pyridine. The film was sulfurized at 575 °C for 2 h.

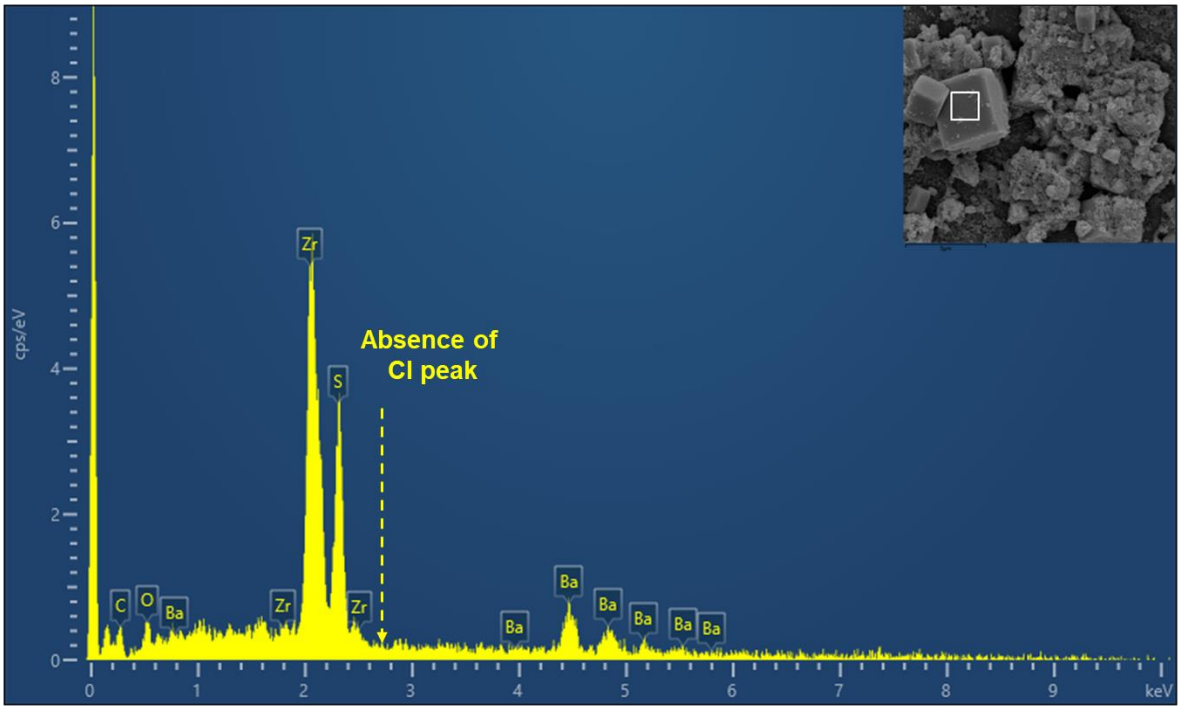

Figure S24. SEM-EDX analysis of $BaZrS_3$ after sulfurization of ZrS_3-BaS stack where ZrS_3 is synthesized from $ZrCl_4$-CS_2-butylamine-pyridine. The film was sulfurized at 575 °C for 2 h. The film does not contain any chlorine.

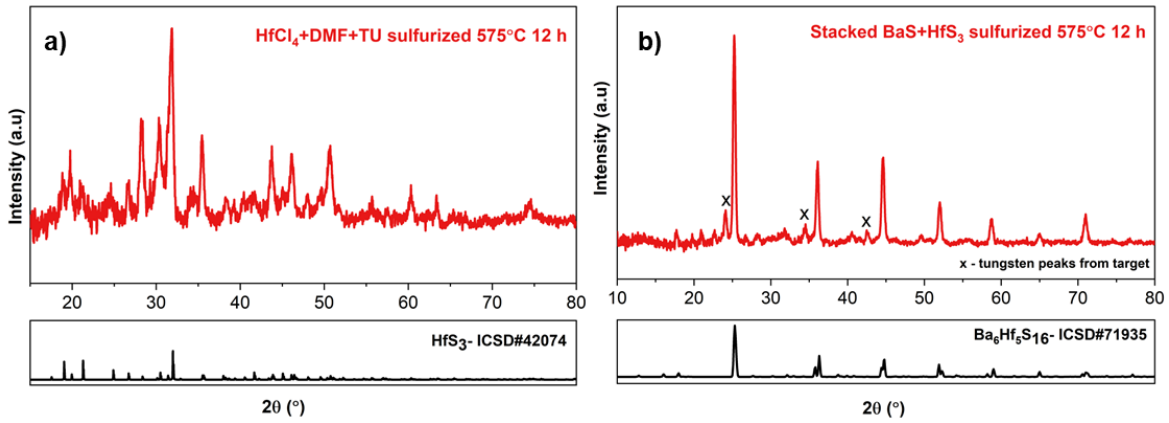

Figure S25. X-ray diffraction plot showing a) the synthesis of HfS_3 from $HfCl_4$-dimethyl formamide (DMF)-thiourea (TU) chemistry at 575 °C for 6 h and b) the synthesis of a Ruddlesden Popper phase of Ba-Hf-S synthesized from a bilayer stack of HfS_3-BaS where HfS_3 was synthesized from $HfCl_4$-dimethyl formamide-thiourea chemistry. The stacked film was sulfurized at 575 °C for 2 h.

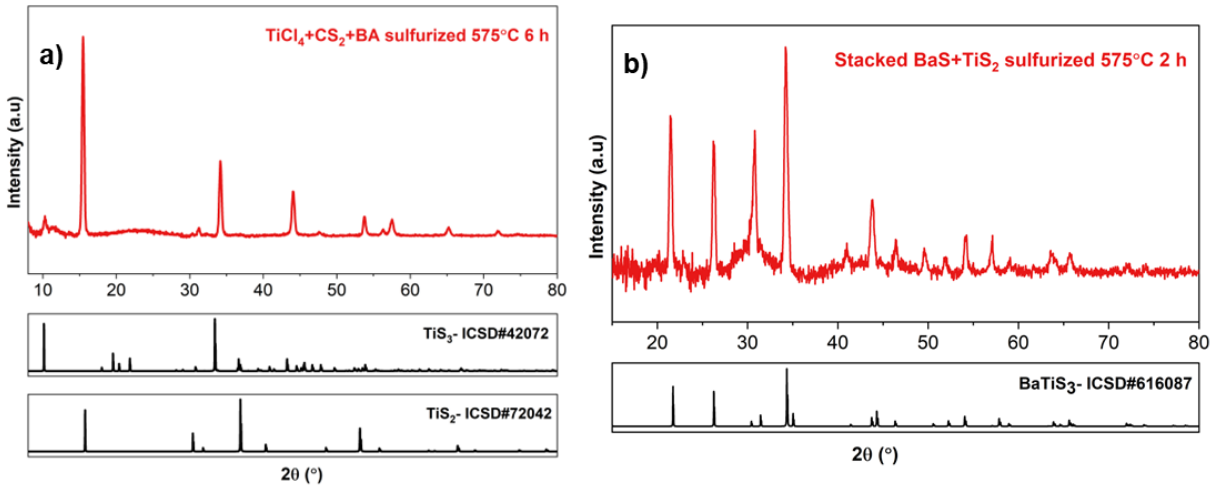

Figure S26. X-ray diffraction plot showing a) the synthesis of a mixture of TiS_3 and TiS_2 from $TiCl_4$-CS_2-butylamine (BA)-pyridine (Pyd) chemistry at 575 °C for 6 h and b) the synthesis of $BaTiS_3$ from a bilayer stack of TiS_2/TiS_3-BaS. The stacked film was sulfurized at 575 °C for 2 h.

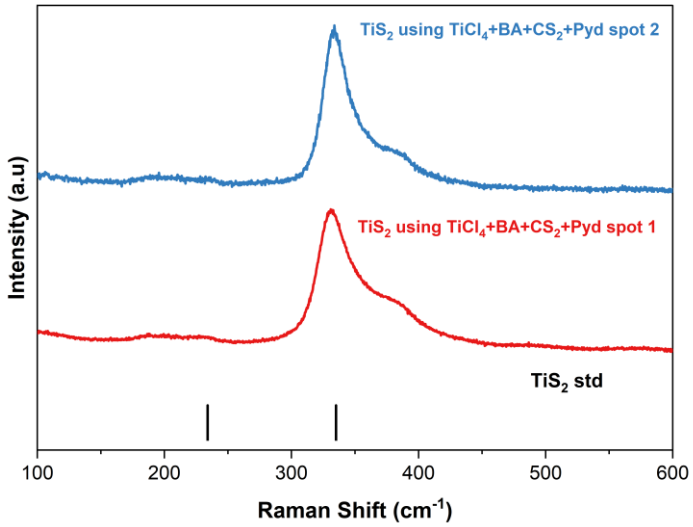

Figure S27. Raman of TiS_2 film synthesized from $TiCl_4$-butylamine (BA)-CS_2-pyridine (Pyd) and sulfurized at 575 °C for 6 h.

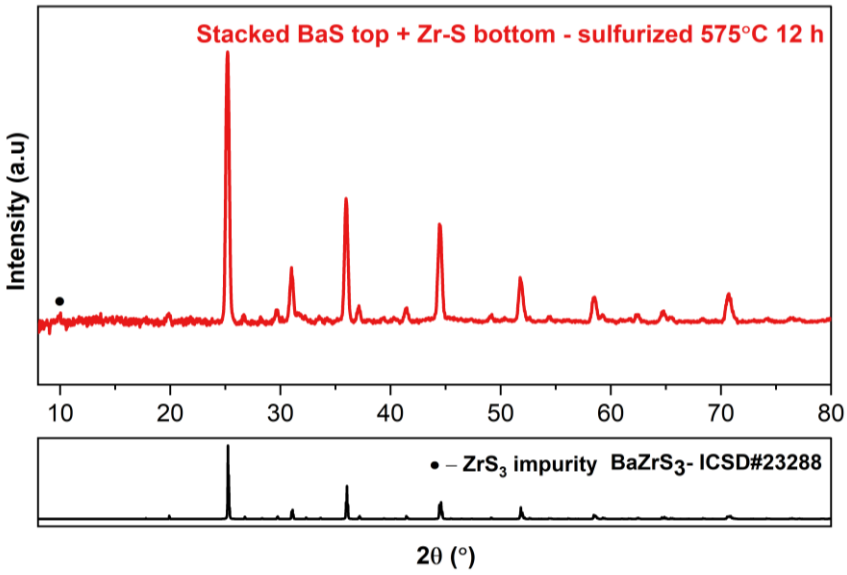

Figure S28. X-ray diffraction pattern of $BaZrS_3$ after sulfurization of as annealed ZrS_x and BaS stack where ZrS_x is synthesized from $ZrCl_4$-butylamine-CS_2-pyridine. The film was sulfurized at 575 °C for 12 h.

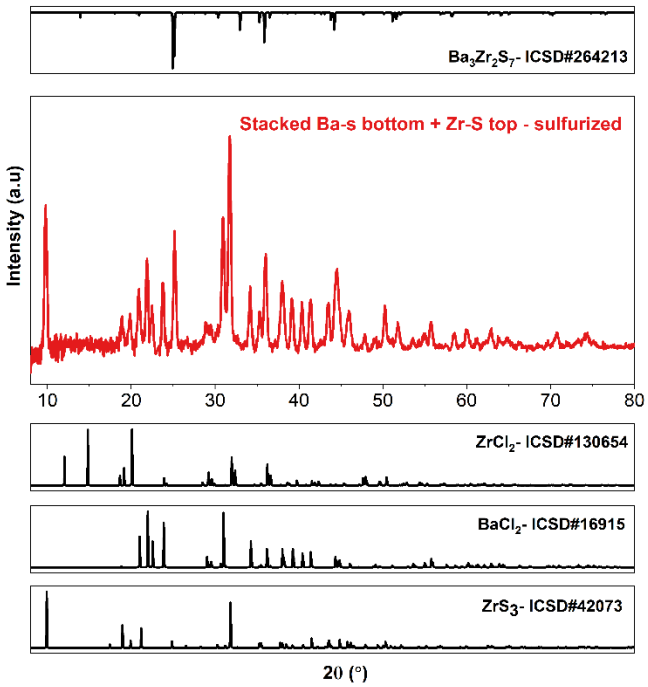

Figure S29. X-ray diffraction pattern confirmed chlorine impurity after the sulfurization of a stack of BaS at the bottom and as annealed ZrS_x at the top where ZrS_x is synthesized from $ZrCl_4$-butylamine-CS_2-pyridine. The film was sulfurized at 575 °C for 12 h and showed a secondary $BaCl_2$ phase.

Hybrid colloidal precursor

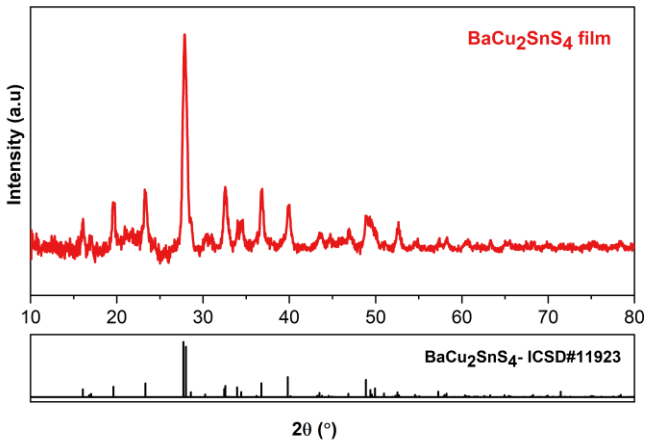

Figure S30. X-ray diffraction pattern of Cu_2BaSnS_4 synthesized from fully dissolved metal sulfides/pure metal precursor ink. Cu_2S, BaS, and Sn powder were dissolved in a mixture of propylamine-CS_2-pyridine to form a 0.4 M total metal concentration ink. The ink was dropcasted at 350 °C and annealed for 10 min.

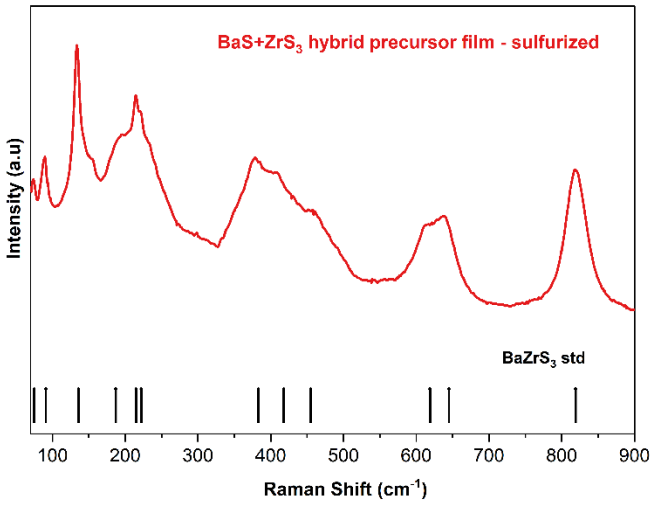

Figure S31. Raman spectra confirmed the synthesis of $BaZrS_3$ from a hybrid precursor ink of dissolved BaS and suspended ZrS_3. The film was sulfurized at 575 °C for 2 h. ZrS_3 was synthesized from sulfurization of Zr nanopowder, resulting in less than 1-micron size grains of ZrS_3. Reference Raman peaks were identified by Pandey et al.[1]

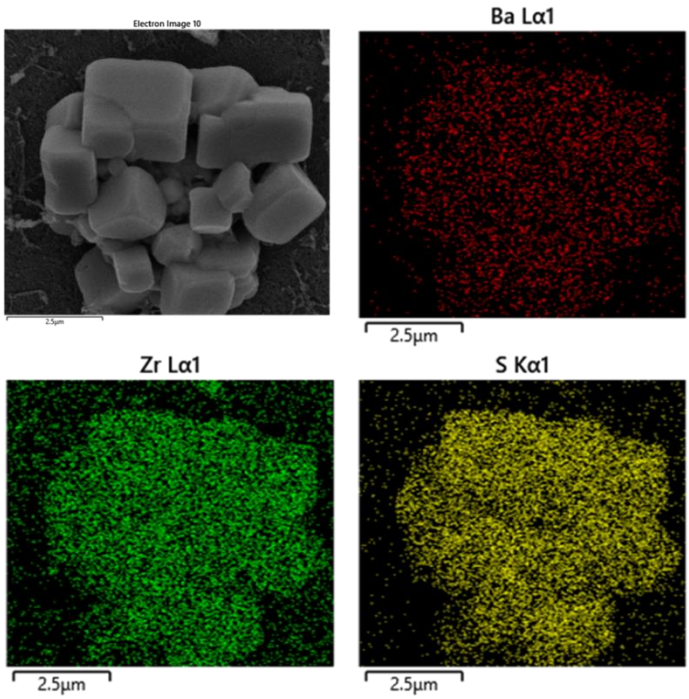

Figure S32. EDX map of $BaZrS_3$ after sulfurization of as-coated film from ZrS_3-BaS hybrid precursor ink. The film was sulfurized at 575 °C for 2 h. ZrS_3 was synthesized from the sulfurization of Zr nanopowder, resulting in less than 1-micron grains of ZrS_3.

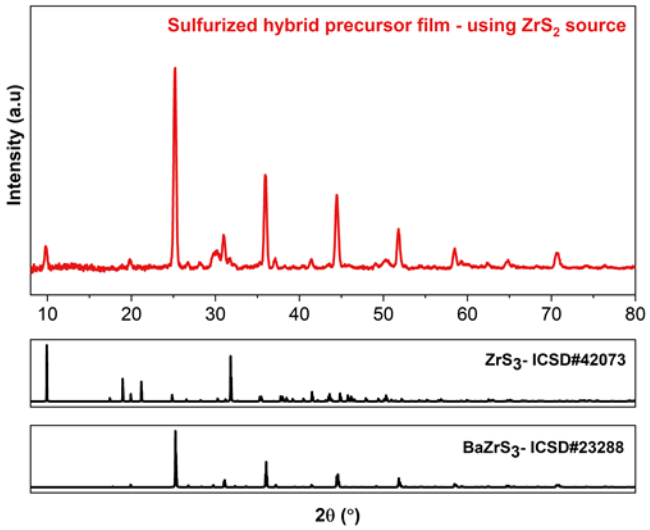

Figure S33. XRD pattern of $BaZrS_3$ after sulfurization of a doctor blade coated ZrS_3-BaS hybrid precursor ink, where ZrS_3 was synthesized from sulfurization of bulk ZrS_2 powder, resulting in large grains of ZrS_3. The film was sulfurized at 575 °C for 2 h and contains unreacted ZrS_3 and BaS_3 along with $BaZrS_3$.

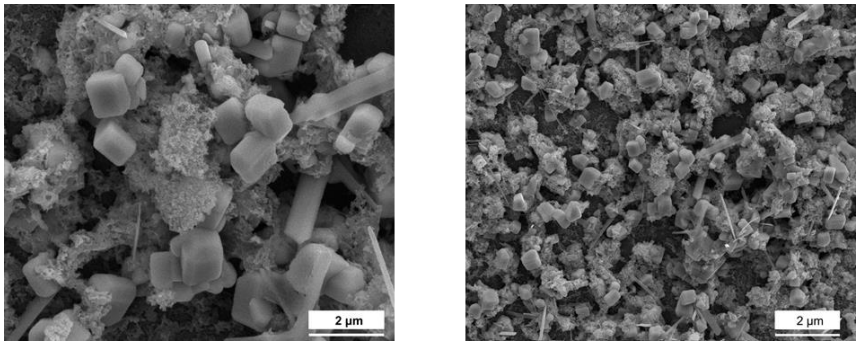

Figure S34. SEM top view of $BaZrS_3$ after sulfurization of a doctor blade coated ZrS_3-BaS hybrid precursor ink, where ZrS_3 was synthesized from sulfurization of bulk ZrS_2 powder resulting in large grains of ZrS_3. The film was sulfurized at 575 °C for 2 h and contains unreacted ZrS_3 and BaS_3 along with $BaZrS_3$.

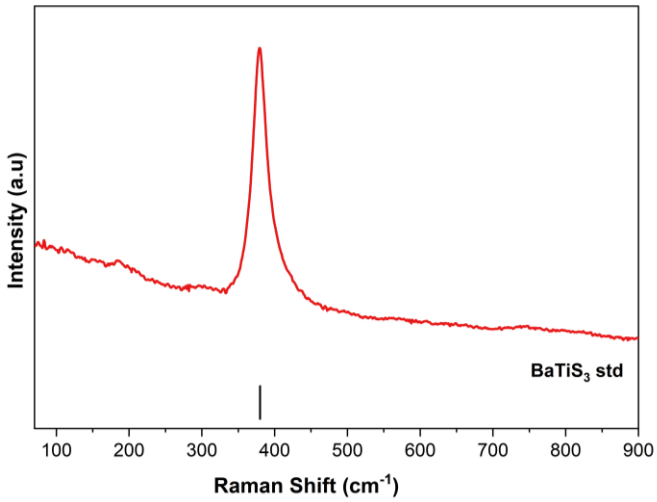

Figure S35. Raman spectra confirmed the synthesis of $BaTiS_3$ from a hybrid precursor ink of dissolved BaS and suspended TiS_2. The film was sulfurized at 575 °C for 2 h. TiS_2 was synthesized from the sulfurization of TiH_2 nanopowder.

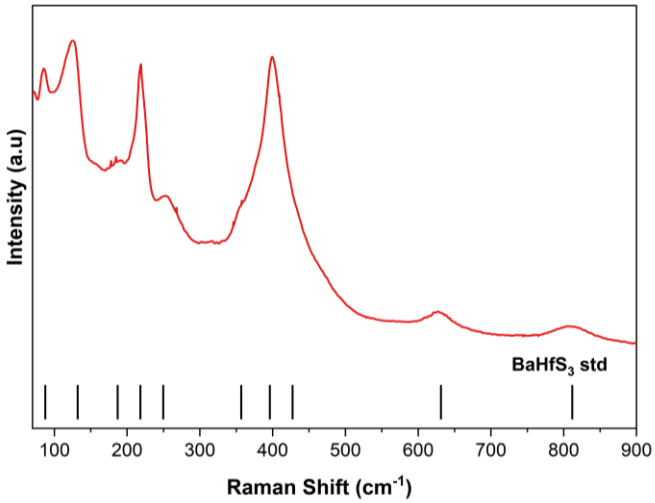

Figure S36. Raman spectra confirmed the synthesis of $BaHfS_3$ from a hybrid precursor ink of dissolved BaS and suspended HfS_3. The film was sulfurized at 575 °C for 2 h. HfS_3 was synthesized from the sulfurization of HfH_2 nanopowder.

Selenium liquid flux

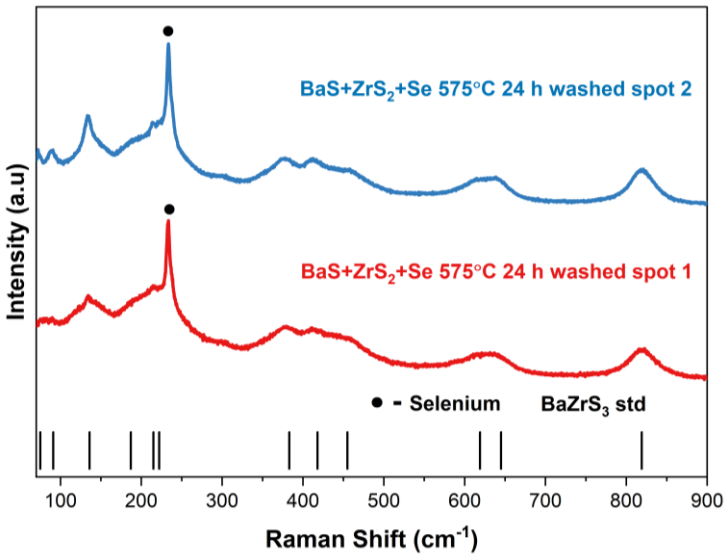

Figure S37. Raman of water-washed $BaZrS_3$ synthesized from Se flux at 575 °C for 24 h. Raman shows that slight impurities of selenium remained in the powder. However, the excess selenium can readily dissolve in an amine-thiol mixture or other solution chemistries. Reference Raman peaks were identified by Pandey et al.[1]

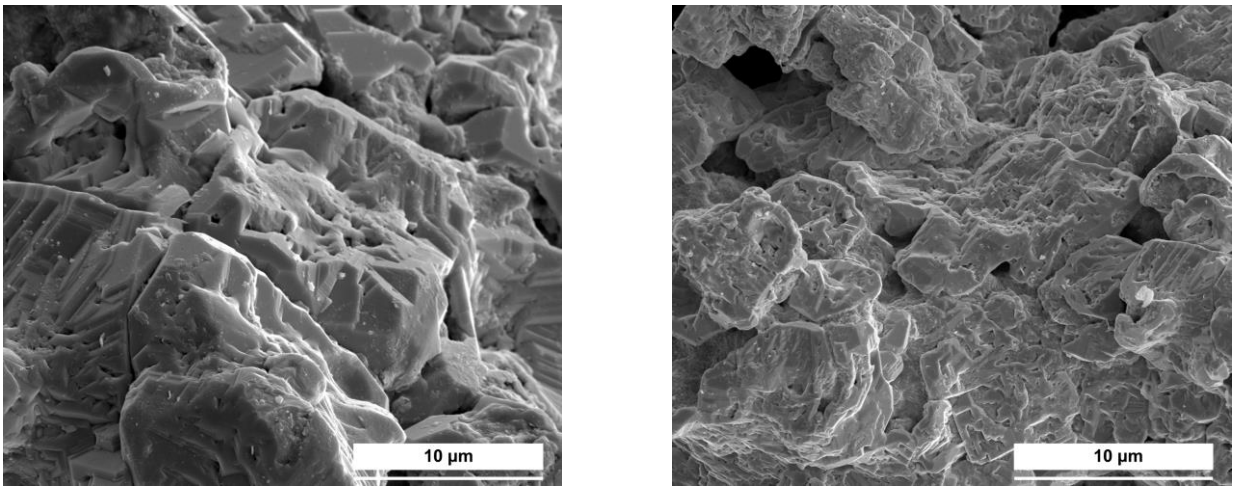

Figure S38. SEM images of water-washed $BaZrS_3$ synthesized from selenium liquid flux at 575 °C for 24 h.

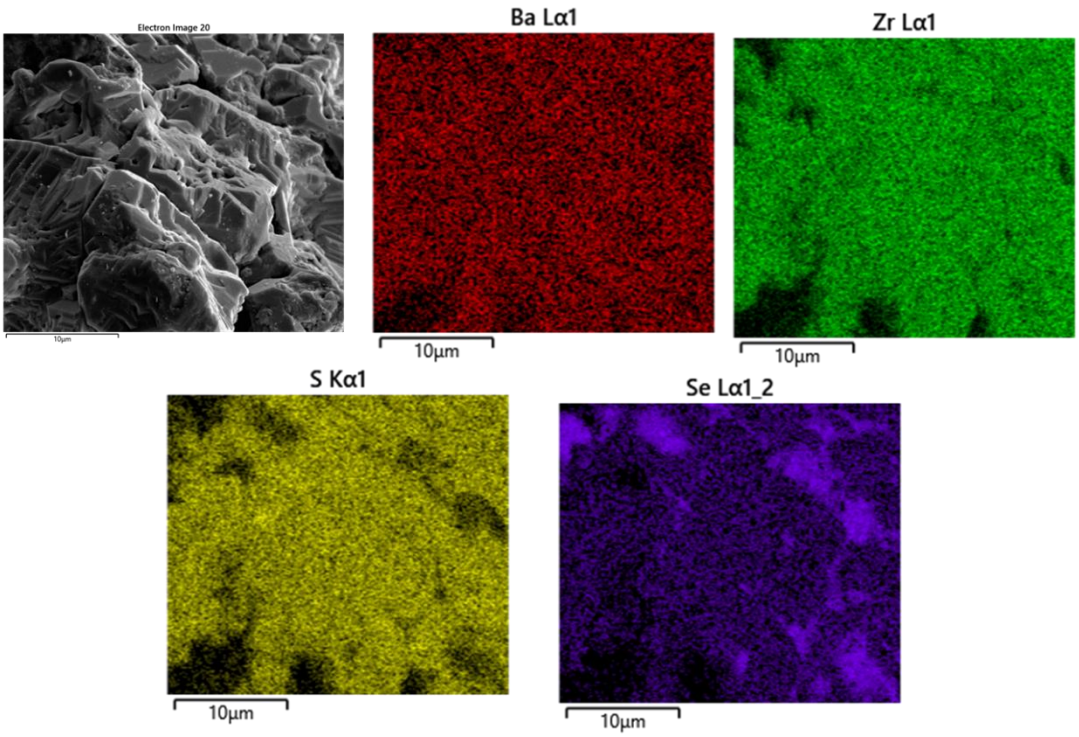

Figure S39. SEM-EDX analysis of water-washed $BaZrS_3$ synthesized from selenium liquid flux at 575 °C for 24 h. The $BaZrS_3$ grains predominantly contain Ba, Zr, and S, with negligible selenium within the grain. However, some pockets of residual bulk selenium remained, which can be removed with a relevant solution treatment.

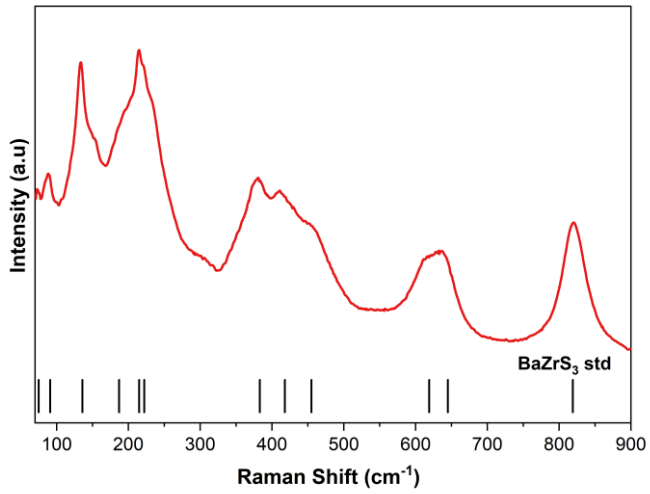

Figure S40. Raman of amine-thiol washed $BaZrS_3$ synthesized from Se flux at 575 °C for 24 h. After the water wash, the $BaZrS_3$ powder was rinsed in a propylamine-ethanedithiol mixture (5:1 vol:vol). The residual selenium was washed away. Reference Raman peaks were identified by Pandey et al.[1]

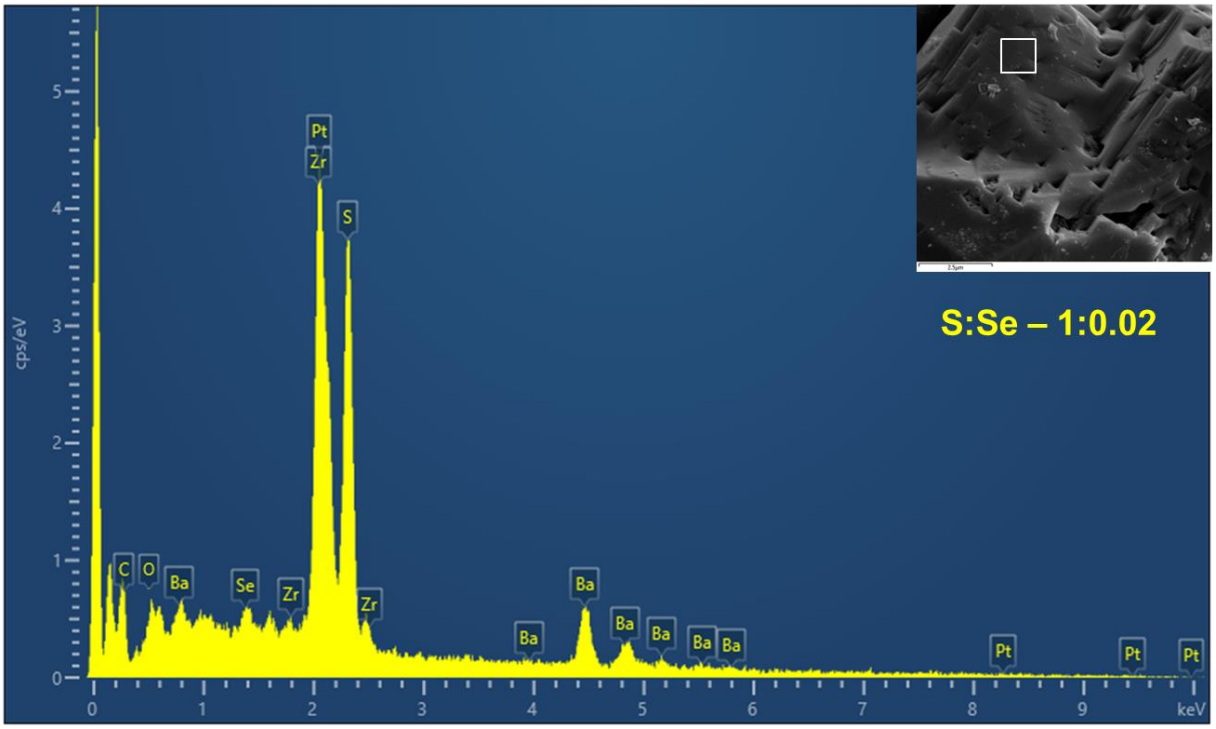

Figure S41. SEM-EDX analysis of water-washed $BaZrS_3$ synthesized from selenium liquid flux at 575 °C for 24 h. The $BaZrS_3$ grains predominantly contain Ba, Zr, and S, with negligible selenium within the grain. After the water wash, the $BaZrS_3$ powder was rinsed in a propylamine-ethanedithiol mixture (5:1 vol:vol). The residual selenium was washed away. However, the EDX analysis shows that the grains are Ba-poor. It might be because some Ba was lost as $BaSe_3$.

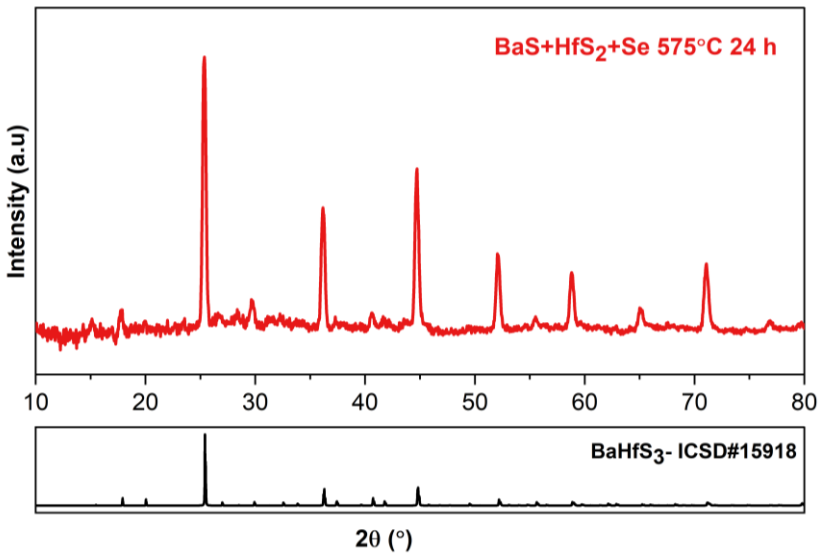

Figure S42. X-ray diffraction plot of water-washed $BHfS_3$ synthesized from selenium liquid flux at 575 °C for 2 h.

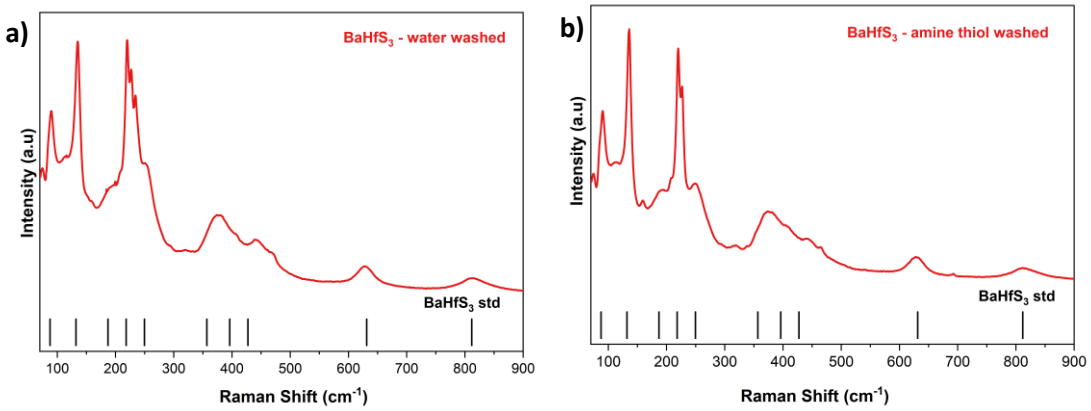

Figure S43. Raman spectra of a) water-washed $BaHfS_3$ and b) propylamine-ethanedithiol-washed $BaHfS_3$ synthesized from selenium liquid flux at 575 °C for 24 h.

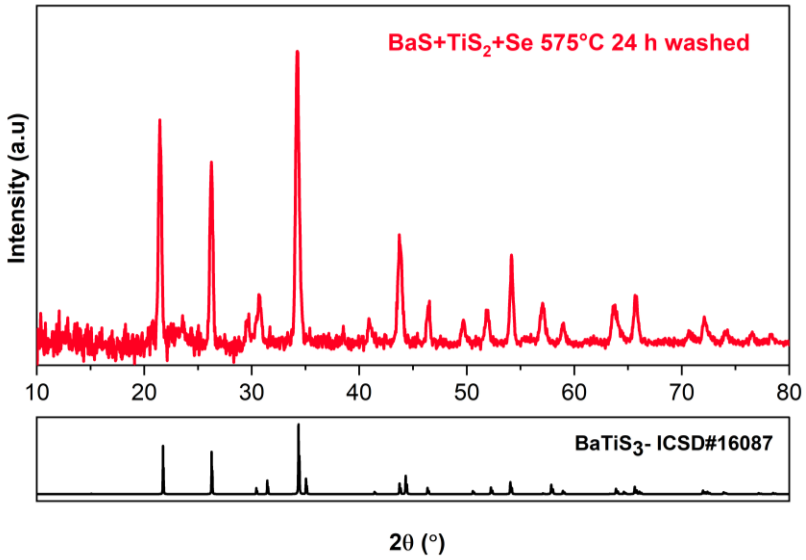

Figure S44. X-ray diffraction plot of water-washed $BaTiS_3$ synthesized from selenium liquid flux at 575 °C for 24 h.

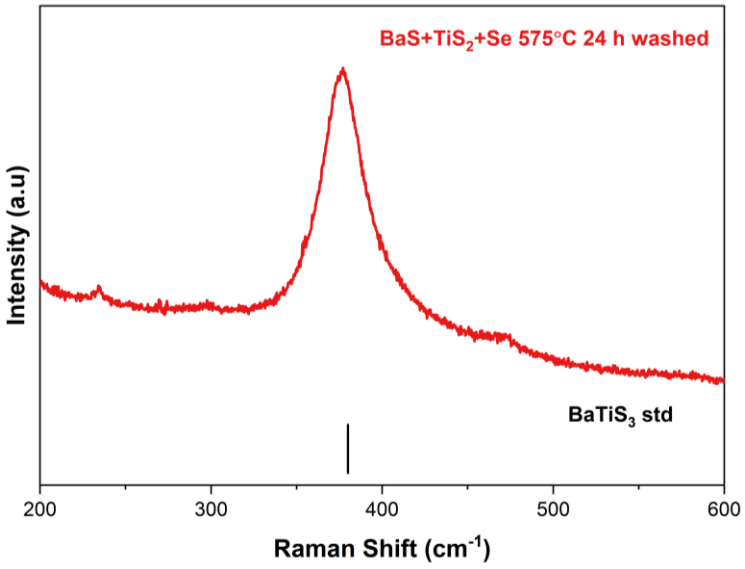

Figure S45. Raman spectra of water-washed $BaTiS_3$ synthesized from selenium liquid flux at 575 °C for 24 h.

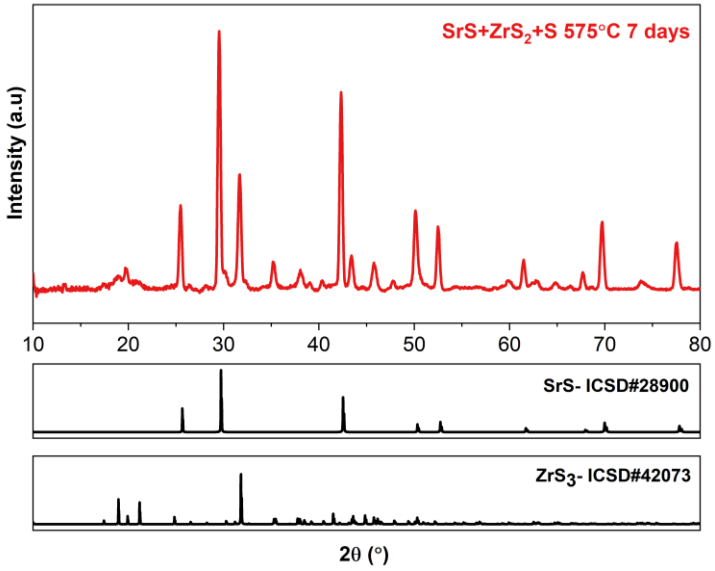

Figure S46. X-ray diffraction plot showing that the heating of the binary sulfides for the potential synthesis of $SrZrS_3$ in the presence of sulfur did not result in a ternary phase even after 7 days

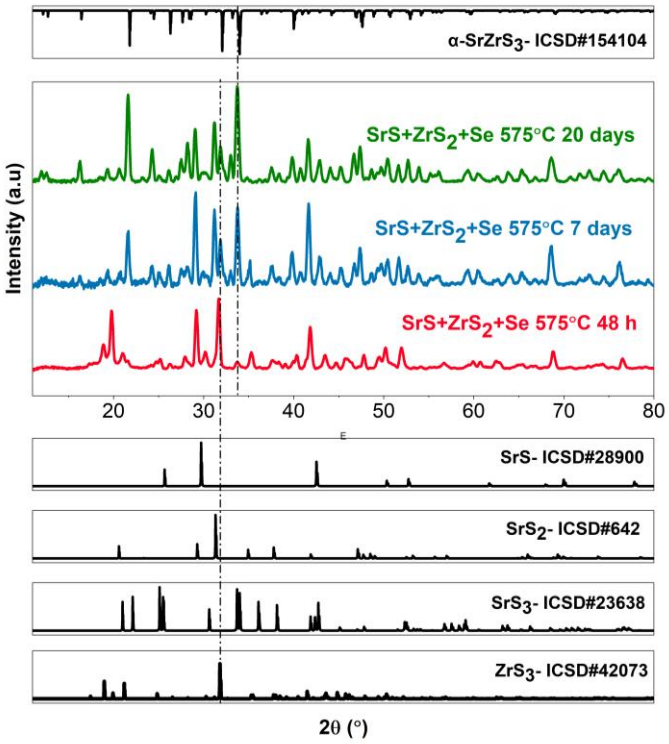

Figure S47. X-ray diffraction plot of the time evolution of α-$SrZrS_3$ phase synthesized using binary sulfides and selenium liquid flux at 575 °C.

References:

(1) Pandey, J.; Ghoshal, D.; Dey, D.; Gupta, T.; Taraphder, A.; Koratkar, N.; Soni, A. Local Ferroelectric Polarization in Antiferroelectric Chalcogenide Perovskite BaZrS3 Thin Films. *Phys Rev B* **2020**, *102* (20), 205308. https://doi.org/10.1103/PhysRevB.102.205308.

(2) Osada, K.; Bae, S.; Tanaka, M.; Raebiger, H.; Shudo, K.; Suzuki, T. Phonon Properties of Few-Layer Crystals of Quasi-One-Dimensional ZrS_3 and $ZrSe_3$. *The Journal of Physical Chemistry C* **2016**, *120* (8), 4653–4659. https://doi.org/10.1021/acs.jpcc.5b12441.